STEM CELLS®

CANCER STEM CELLS

Snail and Slug Mediate Radioresistance and Chemoresistance by Antagonizing p53-Mediated Apoptosis and Acquiring a Stem-Like Phenotype in Ovarian Cancer Cells

NAWNEET K. KURREY,[a] SWATI P. JALGAONKAR,[b] ALOK V. JOGLEKAR,[b] AVINASH D. GHANATE,[b] PRASAD D. CHASKAR,[b] RAHUL Y. DOIPHODE,[b] SHARMILA A. BAPAT[a]

[a]National Centre for Cell Science, NCCS Complex, Pune University Campus, Pune, India; [b]Institute of Bioinformatics and Biotechnology, University of Pune, Pune, India

Key Words. Snail-slug • EMT • Radioresistance and chemoresistance • Ovarian cancer stem cells

ABSTRACT

The transcriptional repressors Snail and Slug contribute to cancer progression by mediating epithelial-mesenchymal transition (EMT), which results in tumor cell invasion and metastases. We extend this current understanding to demonstrate their involvement in the development of resistance to radiation and paclitaxel. The process is orchestrated through the acquisition of a novel subset of gene targets that is repressed under conditions of stress, effectively inactivating p53-mediated apoptosis, while another subset of targets continues to mediate EMT. Repressive activities are complemented by a concurrent derepression of specific genes resulting in the acquisition of stem cell-like characteristics. Such cells are bestowed with three critical capabilities, namely EMT, resistance to p53-mediated apoptosis, and a self-renewal program, that together define the functionality and survival of metastatic cancer stem cells. EMT provides a mechanism of escape to a new, less adverse niche; resistance to apoptosis ensures cell survival in conditions of stress in the primary tumor; whereas acquisition of "stemness" ensures generation of the critical tumor mass required for progression of micrometastases to macrometastases. Our findings, besides achieving considerable expansion of the inventory of direct genes targets, more importantly demonstrate that such elegant cooperative modulation of gene regulation mediated by Snail and Slug is critical for a cancer cell to acquire stem cell characteristics toward resisting radiotherapy- or chemotherapy-mediated cellular stress, and this may be a determinative aspect of aggressive cancer metastases. STEM CELLS *2009;27:2059–2068*

Disclosure of potential conflicts of interest is found at the end of this article.

INTRODUCTION

The classic hallmarks of cancer include growth factor independence, insensitivity to antigrowth signals, evasion of programmed cell death, limitless replicative potential, sustained angiogenesis, and tissue invasion for metastasis [1]. Aggressive tumors selectively enhance these characteristics in progressing to a therapy-refractile state. Over the last decade, failure of cancer therapy has also been attributed to the persistence of quiescent cells called cancer stem cells (CSCs), that inherently express some of these characteristics, but are better recognized through their potential to efficiently regenerate tumor tissue even after therapeutic intervention [2]. The origin of these stem cells in tumors and their resistance to stress are not well delineated; however, they are proposed to arise either from transformation of stem and progenitor cells, or through dedifferentiation of cancer cells [3].

It is increasingly being realized that changes in cellular architecture and polarity affect cell fate of stem cells during development, organogenesis, and cancer. The generation of CSCs from immortalized human mammary epithelia has recently been shown to be triggered by one such process that mediates a change in cell morphology, namely epithelial mesenchymal transition (EMT) [4–6], that involves the loss of cell adhesion and acquisition of migratory and invasive properties by cells [7, 8]. However, the mechanistic understanding of the generation of CSCs through EMT has not yet been delineated, although an association is established.

The Snail family members Snail (*Snai1*) and Slug (*Snai2*) are closely related transcriptional repressors implicated in embryonic development, wherein they have been shown to be vital for the formation of mesoderm and neural crest through their recognized functionality of EMT [9]. In normal tissues of adult organisms, these transcription factors (TFs) are more commonly described in the context of wound healing, or protecting stem/progenitor cells from DNA damage [10]. Slug mediates radioprotective effects and enhanced survival of progenitor cells through activation of the SCF/cKit pathway [11, 12]. In the context of cancer, the current understanding of the

Author contributions: N.K.K. and S.P.J.: collection and assembly of data, data analysis and integration, manuscript writing; A.V.J., A.D.G., P.D.C., and R.Y.D.: data analysis and integration; S.A.B.: conception and design, financial support, collection and assembly of data, data analysis and interpretation, manuscript writing, final approval of manuscript.

Correspondence: Sharmila A. Bapat, Ph.D., National Centre for Cell Science, NCCS Complex, Pune University Campus, Ganeshkhind, Pune 411 007, India. Telephone: 91-020-25708078; Fax: 91-020-25692259; e-mail: sabapat@nccs.res.in, http://www.nccs.res.in/bapat1.html Received March 12, 2009; accepted for publication June 8, 2009; first published online in STEM CELLS *EXPRESS* June 18, 2009. 1066-5099/2009/$30.00/0 doi: 10.1002/stem.154

role of these TFs focuses on their capability to mediate EMT. The acquisition of invasive properties by metastasizing cancer cells and disease progression to a stage associated with adverse prognosis for patients have been frequently attributed to the expression of *Snail* and *Slug* [13–15]. The well-established roles of Snail and Slug in EMT during both embryogenesis and tumor progression reflect their possible participation in migration of cancer stem cells [16]. EMT associated with recurrent wound healing has also been hypothesized as a risk factor in several physiological cancers, for example, in normal epithelial ovarian surface cell transformation [17], intestinal cell transformation [18], and others.

At the molecular level, Snail and Slug mediate gene regulation through recognition and specific binding to consensus sites in the promoter regions of their target genes that contain the core sequence -CANNTG- [19, 20]. This binding is followed by recruitment of factors involved in transcriptional repression including HDAC1, SIN3A, and so on [21]. Despite a strong implication of diverse roles of Snail and Slug in carcinogenesis, the currently known repertoire of direct targets of these TFs is, for the most part, restricted to genes encoding cell junction components. Moreover, since a majority of targets are reportedly repressed by both TFs, it is not known whether the latter play distinct or redundant roles during tumorigenesis; although circumstances suggest that Snail and Slug may modulate some of these targets differentially [12]. We reasoned that elucidation of the diverse functionality of these TFs may be addressed through identification of their complete repertoire of direct targets that could reflect the various processes possibly being regulated. Toward this aim, we applied several major genome-wide analyses: (a) in silico identification of the putative target genes of Snail and Slug in the human genome based on knowledge of the consensus sequence recognized by Snail and Slug, (b) introduction of TF specificity into the analyses by performing chromatin immunoprecipitation and promoter array analysis (ChIP-on-chip) using human genome-wide promoter arrays, and (c) screening of existing gene expression databases and published literature to identify possible additional targets. We thus derived a small subset of target genes that were further validated in a biological consequence, namely radioresistance and chemoresistance in ovarian cancer.

Our approach, besides achieving considerable expansion of the inventory of direct genes targets, and thereby, roles of these molecules in cancer, also suggests a definitive target gene modulation defining the molecular mechanisms mediated by Snail and Slug to overcome radiotherapy- or chemotherapy-mediated cellular stress. In a larger perspective, our findings reveal that these transcriptional repressors are critical for regulation of apoptosis and acquisition of stem-like characteristics by cancer cells.

Materials and Methods

In Silico Whole-Genome Analysis of Snail and Slug Binding Sites

The Human genome (build 36.1 reference assembly: ftp://ftp.ncbi.nih.gov/genomes/H_sapiens/ARCHIVE/BUILD.36.1) was used as the source for extracting the gene table information in conjunction with the gene sequences from FASTA formatted files; this constituted the primary database. We proceeded to extract a secondary database (consisting of 2-kb upstream to 1-kb downstream sequences from the transcription start site of all genes), and a tertiary database specific for the Snail and Slug binding site sequences, namely CACCTG and CAGGTG. A final list composed of 14,532 genes and corresponding number of E-boxes in their promoter regions was thus generated (supporting information Table 1, Fig. 1).

ChIP-on-chip and ChIP polymerase chain reactions

ChIP, combined with microarray analysis, was performed as described earlier [22]. The corresponding genes for the probes bound by Snail and/or Slug as identified through this effort are listed in supporting information Table 2. The calculation of percentage of target genes is based on the number genes with E-boxes in their promoter regions (5,677) of the total of 14,633 annotated genes on the arrays. Functional classification of these genes was carried out using gene expression analysis tool of PANTHER (Protein ANalysis THrough Evolutionary Relationships: http://www.pantherdb.org/tools/compareToRefListForm.jsp), which classifies genes by their functions; pathways indicated to be significant ($p < .005$) were identified and are represented in supporting information Figure 1. Promoter regions were amplified in immunoprecipitated chromatin by polymerase chain reaction (PCR) amplification using primers designed to specifically amplify the E-boxes within promoter regions of these genes; sequences are available on request. Amplified products were run on 1.8% agarose gel and band intensities measured by densitometric analysis using Genetool3.6 (Syngene, Cambridge, England, http://www.syngene.com).

Cell Culture and Establishment of Cell Systems

All cultures were maintained in minimum essential medium (E) plus 5% fetal calf serum and 1% nonessential amino acid solution at 37°C in 5% CO_2 incubator. A4 cells (an epithelial ovarian cancer cell line developed earlier in our lab [3]) were used as the parental cell line for studies. Stable transfectants of A4 cells overexpressing Snail and Slug (SNA and SLA, respectively), radioresistant A4 cells (AR), paclitaxel-resistant A4 cells (AC), and transient Snail and Slug knockdown (siRNA Smartpool for Snail and Slug; procured from Dharmacon Inc., Chicago, http://www.dharmacon.com) were developed using standard procedures. SNA, SLA, AR, and AC demonstrated a typical fibroblast-like appearance characteristic of EMT compared with the parental epithelial A4 cells (supporting information Figs. 4B, 6A).

Data Mining from Gene Expression Databases

Gene expression dataset analyses relating to Snail and Slug available in the public domain (Gene Expression Omnibus [23]) and published literature [15, 24-26] were meticulously scanned to identify genes possibly regulated by these two TFs. This effort generated a subset of 340 genes (supporting information Table 3) that are differentially modulated by Snail and Slug, although the nature of their interactions—whether through direct promoter binding or systems networks involving other components—is not known. Further overlapping the three gene lists generated a small subset of 64 E-box-containing promoters for wet-lab validation (supporting information Table 3, marked in red).

RNA Extraction and Reverse-Transcriptase PCR

Total RNA was extracted from cells using Trizol—2 μg of which was reverse-transcribed into cDNA, and amplified for 30 cycles. Each cycle comprised 45-second denaturation at 94°C, 45-second annealing at the appropriate temperature midpoint standardized for each primer set, and 45-second extension at 72°C. β-actin was used as internal control in all reactions. Amplification was quantified by running amplicons on a 1.5% agarose gel and measuring band intensities as described above.

Immunoblotting

Total cellular protein was extracted in RIPA lysis buffer and estimated using DC protein estimation kit (Bio-Rad, Hercules, CA, http://www.bio-rad.com). Protein was denatured by heating at 95°C for 2 minutes, resolved on 10%–15% denaturing SDS-polyacrylamide gel electrophoresis, transferred onto a Hybond nitrocellulose membrane (semidry transfer; 20 V for 45 minutes),

blocked, and incubated overnight with primary antibody. After three buffer washes, the blot was exposed to horseradish peroxidase-conjugated secondary antibody for 3 hours, washed, and developed using Pierce SuperSignal West Pico chemiluminescence substrate (Pierce, Rockford, IL, http://www.piercenet.com).

Immunostaining for TUNEL

Coverslip-grown cells were fixed in 4% paraformaldehyde, permeabilized (0.1% Triton X-100 in 0.1% sodium citrate made in phosphate-buffered saline), and incubated either with or without dTT (dithiotreitol) enzyme containing terminal deoxynucleotidyl transferase-mediated dUTP-biotin nick-end labeling (TUNEL) mixture (Roche Diagnostics GmbH, Mannheim, Germany, http://roche-applied-science.com) at 37°C for 1 hour. Analysis for apoptosis was determined by images captured on a confocal microscope (Carl Zeiss, Jena, Germany, http://www.zeiss.com).

Flow Cytometry Cell Analysis

For cell cycle analysis, cells were harvested, fixed with chilled 70% ethanol for 15 minutes, washed in buffer, and stained with 50 μg/ml propidium iodide and 1 mg/ml RNase (Type IIA; Sigma-Aldrich, St. Louis, http://www.sigmaaldrich.com) for 30 minutes at 37°C. For TUNEL assay, cells were fixed in 4% paraformaldehyde and permeabilized as above, incubated either with or without dTT enzyme containing TUNEL Mixture (Roche Biosciences) at 37°C for 1 hour. Events were acquired on BD FACSCaliber (Becton, Dickinson and Company, Franklin Lakes, NJ, http://www.bd.com) and analyses carried out using Cellquest Software (Pro-Beckman Coulter, Krefeld, Germany, http://www.beckman.com).

Clonogenicity Assay (Soft Agar Assay)

In vitro tumorigenecity and anchorage-independent growth were assayed using standard methods. Cells were harvested and suspended in culture medium. One percent agarose was coated onto 35-mm plates, and further overlaid with cell suspension (5,000 cells in 0.5% agarose). Plates were incubated in humidified tissue culture incubator at −37°C, 5% CO_2, for 3 weeks. Visible colonies were counted under a phase-contrast microscope.

Statistical Analysis

Unless mentioned otherwise, all experiments were done in triplicates and data are represented as mean ± SE. Paired *t* test was performed (SigmaStat software; Aspire Software International, Ashburn, VA, http://www.aspiresoftwareintl.com) to determine significant differences between the groups.

RESULTS

Genome-Wide Analysis of Snail and Slug Binding Sites

The probabilistic frequency of the Snail and Slug consensus binding site known as E-box (5′-CANNTG-3′) is 1 in 2,048. With the human genome being ~3.2 billion base pairs [27], several genes are expected to have an E-box in their promoter region. Our in silico analyses for comprehensive genome-wide identification of E-boxes listed 14,532 genes as having an E-box in their promoters (Fig. 1A; supporting information text; supporting information Table 1). The chromosome-wise distribution of these genes (Fig. 1B) indicated that promoters with two or three E-boxes are more frequent; few promoters are associated with more than five E-boxes (a maximal number of 64 E-boxes was found in *Grk1* promoter), whereas some chromosomes had several promoter regions lacking E-boxes (~25% genes in chromosomes 1, 7, 9, 10, 11, 18, and X). This range of frequency distribution of E-boxes, from a total absence to very large numbers, suggests that E-box occurrence is not entirely random in the genome.

To filter this list of gene targets using Snail and/or Slug specificity in the above identification scheme, we carried out ChIP-on-chip to further screen for targets in an epithelial ovarian cancer cell line A4 (established earlier in our lab from tumor ascites of a patient with serous epithelial ovarian carcinoma [3]). Based on a minimum of twofold increased intensity over input DNA, 3,522 genes (Fig. 1C; supporting information Table 2) were identified to be direct targets of either Snail (10.82% targets), Slug (38.19%), or both (13.04%). Functional analyses of these targets indicated that cellular processes of development, metabolism, chromatin modification, cell signaling, and cell adhesion were regulated through common targets; genes involved in chromatin remodeling were targeted by Snail and Slug on an individual level, whereas Slug alone appears to be involved in the regulation of cell cycle and metastasis. Despite this incremental understanding, we realized that the list thus generated could not be considered a true representation of the complete target repertoire, since some of the genes classically regulated by these TFs, including *CDH1*, *CLDN4*, *ITGB1*, and so on, were markedly absent. This inconsistency was attributed to the absence of E-boxes in the probes used on the commercial microarrays.

Guided by a motive of extracting tissue- and disease-specific gene expression patterns implied to be regulated by Snail and Slug toward a specific biological function, namely radioresistance or chemoresistance in ovarian cancer, we further undertook extensive mining of gene expression analyses data relating to these two TFs from public databases and published literature. This effort generated a second list of 340 genes (supporting information Table 3), some of which were further eliminated based on an absence of E-boxes in their promoters or upregulated expression levels. The latter is suggested to indicate either an indirect derepression effect or direct induction through an unknown mechanism [28]. Overlapping the three gene lists identified in the three methodologies described finally yielded a small subset of 64 E-box-containing gene targets (supporting information Table 3, marked in red) for wet-lab validation in ovarian cancer.

Differential Affinities of Snail and Slug in Binding to Certain Gene Promoters and Their Dynamic Modulation in Steady-State and γ-Irradiated Ovarian Cancer Cells

ChIP-PCRs using Snail or Slug antibodies to immunoprecipitate chromatin and specific primers designed to amplify E-boxes in the promoters of the 64 putative targets in the epithelial ovarian cancer cell line (A4) revealed a common set of 37 gene targets for the two TFs. Although the binding affinities were comparable for 12 gene promoters including the known classic targets of these genes, namely *CDH1*, *CLDN4*, *OCLDN*, *KRT18*, and so on (Fig. 2A), the individual targeting efficiencies of the two TFs varied for the remaining genes. A novel finding revealed through statistical analysis of their differential affinities (ratio of Snail/Slug binding) is the increased affinity of Snail for *TP53* and *BRCA2*, whereas Slug expressed a preferential binding to *ITGB1*, *CAV1*, *MUC1*, and *HOOK1* promoters.

We further probed whether the same target profile would be retained or altered in these cells under environmental stress such as exposure to γ-irradiation (LD50 dose was established as 20 Gy for 36 hours; supporting information Fig. 2A, 2B). Using ChIP-PCR assays, a total of 39 targets were identified in the irradiated A4 cells (A4i) that were common to both TFs (Fig. 2B; supporting information Fig. 5A; supporting information

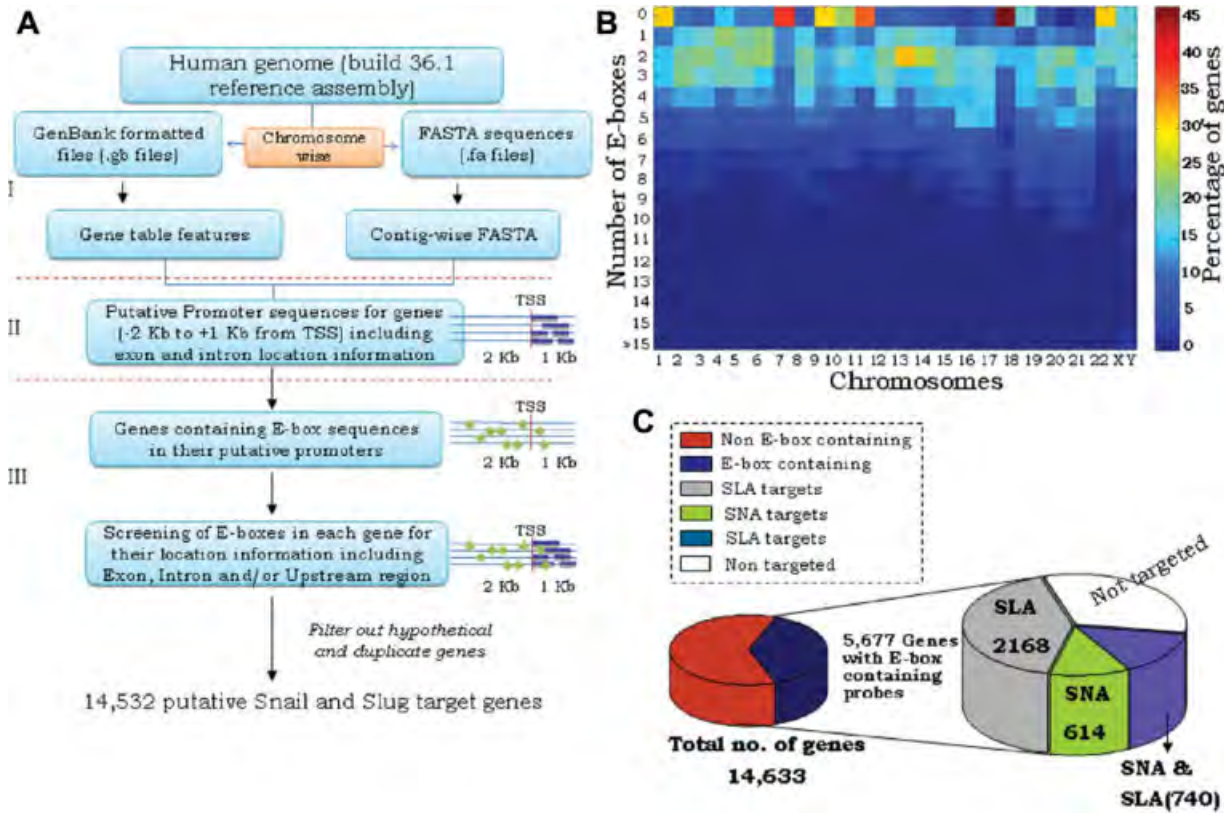

Figure 1. Genome-wide analysis of Snail and Slug binding sites in silico.**(A):** Outline of the computational approach used for genome-wide search of genes containing E-boxes in their putative promoter region. **(B):** Chromosome-wise distribution of genes with respect to the number of E-boxes in the putative promoter region represented as a pseudocolor plot. Chromosomes are represented on the *x*-axis; number of E-boxes, on the *y*-axis. The color of each cell indicates the percentage of genes containing E-boxes in putative promoter regions (−2 kb + 1 kb from TSS). **(C):** Summary of the genes enriched on the 244k promoter arrays by chromatin immunoprecipitation and promoter array analysis using Snail- or Slug-specific antibodies. Shown on the left is the distribution of E-box-containing and noncontaining genes; the pie on the right represents the distribution of Snail, Slug, and Snail-Slug common targets. Abbreviations: SLA, stable transfectants of A4 cells overexpressing Slug; SNA, stable transfectants of A4 cells overexpressing Snail; TSS, transcription start site.

Table 4). A majority of the 20 targets that were retained from steady-state A4 cells had increased binding affinity (*CDH1*, *CLDN4*, *KRT18*, *CAV1*, *BRCA2*, *MMP9*, *SNAI1*, *SNAI2*, and *TP53*); 19 genes emerged as novel targets in the irradiated state that could be significant either in cell survival (*BBC3*, *BCL2*, *EPHA2*, *BID*, *CDNK1A*) or in gene regulation (*SIN3A*, *MAPK3*, *CTNNA1*, *CTNNB1*); whereas 17 targets (*NANOG*, *HDAC1*, *HDAC3*, *CLDN3*, *OCLN*, *MUC1*, *MMP9*, etc.) were lost on irradiation (Fig. 2B; supporting information Fig. 5A). These results suggest a definitive modulation of the direct targets of these molecules under conditions of radiostress.

Profiling for Snail and Slug targets in ectopically overexpressing Snail and Slug A4 clones (SNA and SLA, respectively; supporting information text; supporting information Fig. 4A, 4B) identified a perfect overlap of 28 genes—a reduction in the number of targets from steady-state A4 cells (supporting information Fig. 5B). Twenty-five of these targets were retained from steady state—albeit with varying binding affinities; three novel targets (*MAPK3*, *BBC3*, *PKP2*) were gained (supporting information Table 3), whereas 12 targets at steady state, including *NANOG*, *HDAC1*, *HDAC3*, *MMP9*, and so on, known to contribute to tumorigenesis were lost (Fig. 2Ci). Exposing SNA and SLA cells to γ-irradiation (SNAi and SLAi cells, respectively) generated 16 novel targets including *CCND2*, *CDNK1A*, *BCL2*, *KLF4*, and so on (Fig. 2Cii; supporting information Fig. 5C), whereas 15 genes were retained from steady state (supporting information Table 4). A shift in binding preference was noted for the genes *BRCA2* and *RIN1* to Snail in SNAi cells after irradiation from earlier preferential binding to Slug in SLA cells (Fig. 2Cii; supporting information Fig. 5C). Binding to *HOOK1*, *KRT19*, *TP53*, and *PKP2* promoters was lost on γ-irradiation, possibly indicating derepression of these genes.

To identify target promoters bound at the natively elevated dosages of both TFs in the radioresistant AR cells (developed to resist up to 10 Gy γ-radiation; supporting information Fig. 3), ChIP-PCRs were carried out using Snail- or Slug-immunoprecipitated chromatin (ARSN and ARSL, respectively). Twenty-eight gene targets were thus identified—25 being retained from steady state (Fig. 2Di; supporting information Fig. 5D; supporting information Table 3); 3 novel (*BBC3*, *EPHA2*, and *ITGB1*) and 12 gene targets were lost including *NANOG*, *HDAC1*, *HDAC3*, *MMP9*, and so on, suggesting their derepression. Enhanced promoter binding of *Hook1* to Snail and *TP53*, *CRB3*, and *BRCA2* to Slug was evident in AR cells (supporting information Fig. 5D). Exposure of AR cells to γ-irradiation led to a further modulation of 28 targets (Fig. 2Dii; supporting information Table 4), with emergence of 11 novel targets (*BCL2*, *CASP9*, *CDNK1A*, *PCNA*, etc.) associated with cell survival (supporting information Fig. 5E). A few genes were retained from steady state, whereas seven genes, including *SMAD4*, *ITGB1*, *LAMA3*, *SPP1*, *TIMP3*, *CLDN7*, and *PLAU*, were lost on irradiation possibly indicating a derepression as above (Fig. 2Dii).

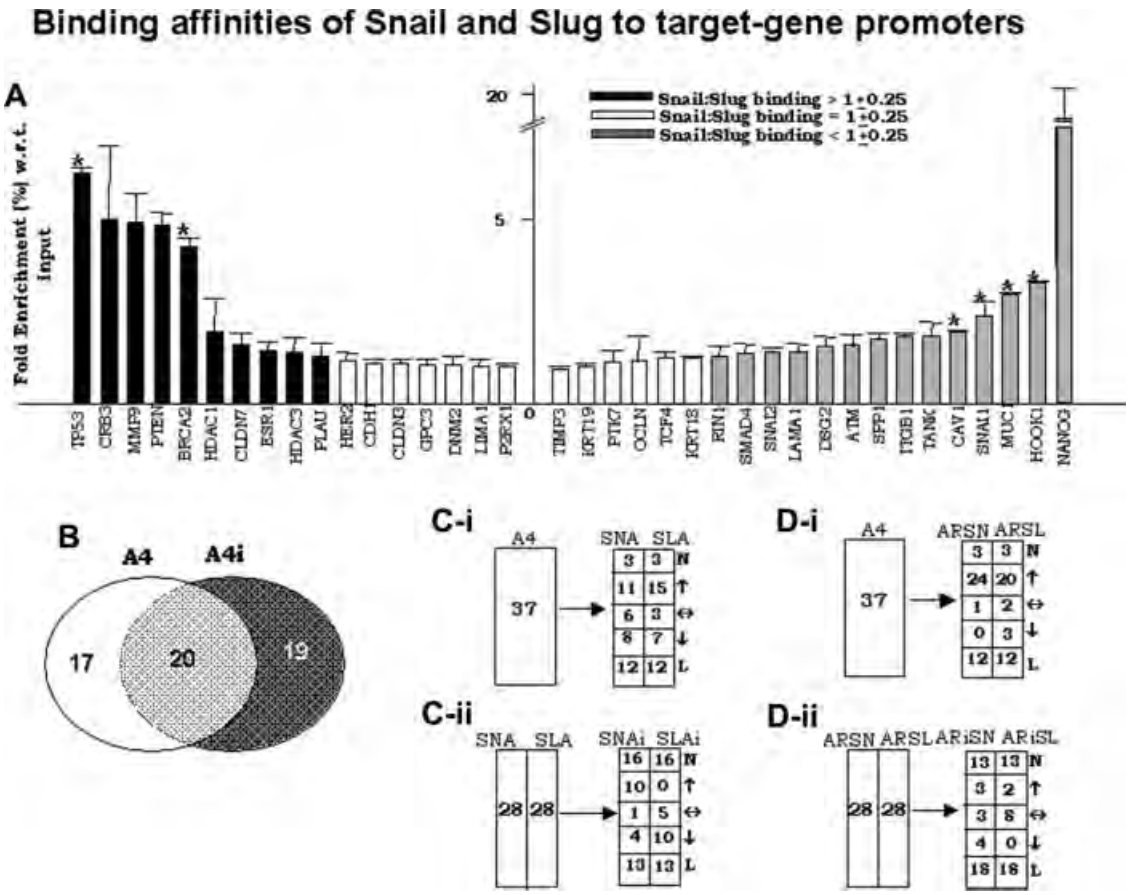

Figure 2. Modulation of gene targets by Snail and Slug in different cell systems. **(A):** Binding of Snail and Slug to target gene promoters in steady-state A4 cells detected by chromatin immunoprecipitation polymerase chain reaction (PCR) assay. Fold enrichment refers to ratio of PCR amplification (determined by densitometry) in Snail pull down versus Slug pull down for the same gene promoter. Each amplification value was initially normalized with that of the input sample; statistical significance was determined using paired *t* test (p value $< .05$). **(B):** Venn diagram showing novel, retained gene targets in γ-irradiated A4 over parental A4 cells. **(Ci):** Panel indicates the target modulation by Snail and Slug in SNA and SLA cells pulled down with Snail- or Slug-specific antibody, respectively, compared with steady-state A4 cells (total 37 targets). **(Cii):** Panel indicates the target modulation by Snail and Slug in SNA and SLA cells immunoprecipitated with Snail- or Slug-specific antibody, respectively, in postirradiated cells (SNAi and SLAi cells, respectively), compared with steady-state SNA and SLA cells (total 28 targets). **(Di):** Panel indicates the target modulation by Snail and Slug in AR cells immunoprecipitated with either Snail- or Slug-specific antibody, respectively (ARSN and ARSL cells, respectively), compared with steady-state A4 cells (total 37 targets). **(Dii):** Panel indicates the target modulation by Snail and Slug in ARSN or ARSL postirradiated cells (referred to as ARiSN and ARiSL cells, respectively), immunoprecipitated with Snail- and Slug-specific antibody, compared with steady-state ARSN/ARSL, respectively (total 28 targets). Denotations: number of targets that were novel (N), retained with enhanced (↑)/equal (↔)/reduced (↓) binding efficiencies, or lost (L). Abbreviations: ARiSL, ARSL postirradiated cells; ARiSN, ARSN postirradiated cells; ARSL, Slug-immunoprecipitated chromatin; ARSN, Snail-immunoprecipitated chromatin; SLA, stable transfectants of A4 cells overexpressing Slug; SLAi, SLA cells exposed to γ-irradiation; SNA, stable transfectants of A4 cells overexpressing Snail; SNAi, SNA cells exposed to γ-irradiation; w.r.t., with respect to.

Upregulation of Snail and Slug in Ovarian Cancer Cells Is Associated with Enhanced Cell Survival and Acquisition of Radioresistance

To test more directly and unambiguously for protective effects of these TFs in cancer cells, we used a comprehensive cell system composed of A4, SNA, SLA, and AR (supporting information Fig. 3). The latter were seen to acquire a native overexpression of Snail and Slug during the development of radioresistance (supporting information Fig. 4C–4E) that supported our hypothesis of a positive association of Snail and Slug with the resistant phenotype. Exposure of these four cell types to γ-irradiation elevated Snail and Slug mRNA and protein levels (Fig. 3A). The concurrent repression of the Snail and Slug target *CDH1* in all cell systems compared with the parental cells is indicative of the functional activity of these TFs.

Cell cycle and survival analyses of the above cell types indicated that A4, SNA, and SLA cells exhibited similar cell cycle kinetics, whereas AR cells had a distinctive profile, with a majority of cells being in G2/M phase and a small fraction of cells being aneuploid (Fig. 3B). On exposure to γ-radiation, a high fraction of all cells tend to accumulate in the G2/M phase. Strikingly, a third of the irradiated parental A4 accumulated in the sub-G0 phase (indicative of DNA fragmentation and apoptosis). Confocal images and flow cytometry data of cells assayed for TUNEL revealed that on exposure to γ-irradiation, a significantly high fraction of A4 cells, moderate numbers of SNA, and minimal fractions of SLA and AR populations were seen to be apoptotic (Fig. 3C, 3D) with respect to parental cells. Further profiling long-term functionality using in vitro soft agar colony-formation assays showed that, whereas at steady state elevated levels of Snail and Slug in the SLA, SNA, and AR

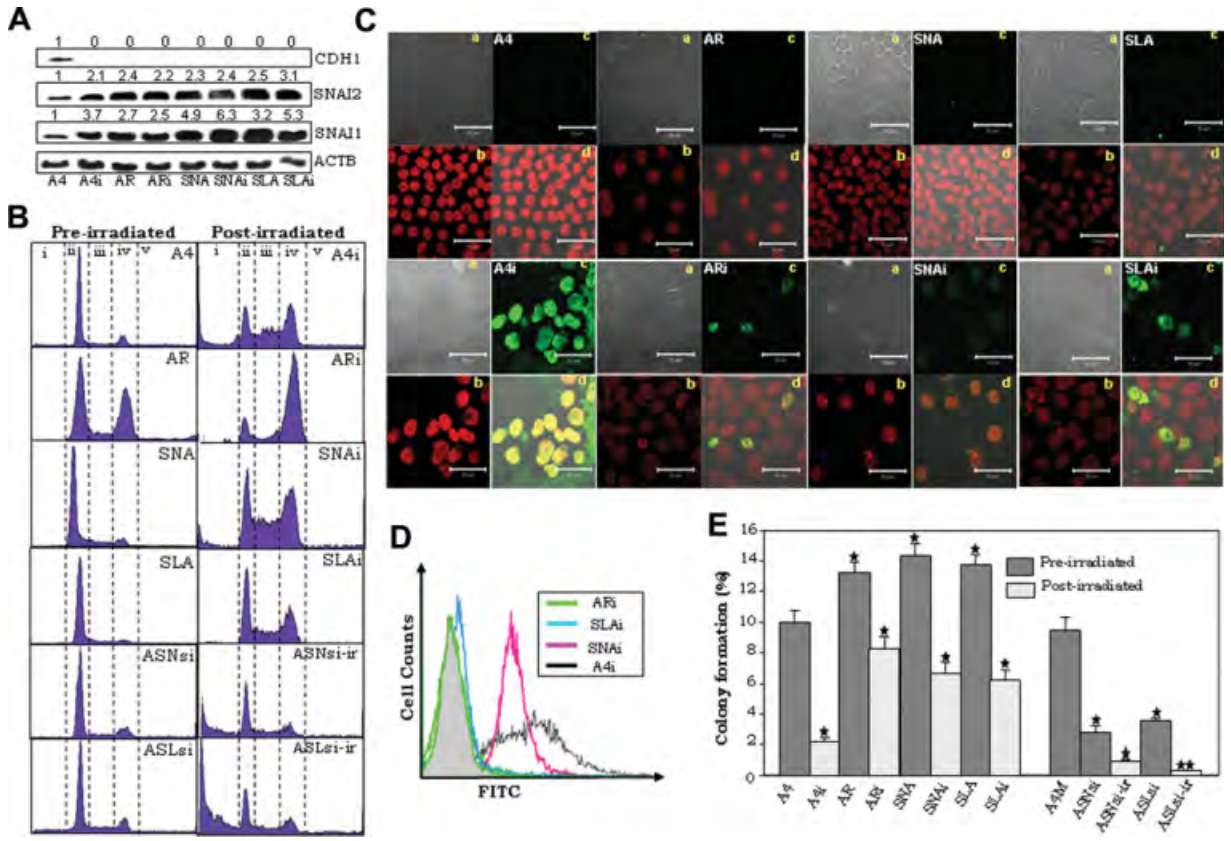

Figure 3. Radioprotective role of Snail and Slug against apoptosis. **(A):** Western blotting analysis of Snail, Slug, and E-cadherin (CDH1) expression in A4, AR, SNA, and SLA cells at steady state and on γ-irradiation (20 Gy for 36 hours: A4i, ARi, SNAi, and SLAi, respectively). ACTB was used as a loading control. Numbers on panel represent the ratio of densitometric value of each band normalized with reference to the loading control, compared with parental A4 control expression. **(B):** DNA content profiles captured through propidium iodide (PI) staining of A4, SNA, SLA, AR, ASNsi, and ASLsi cells at steady state and on γ-irradiation (20 Gy for 36 hours). In each histogram, panels **(i), (ii), (iii), (iv),** and **(v)** represent sub-G0, G0/G1, S, G2/M, and aneuploid cell populations, respectively. **(C, D):** Confocal images and plot overlay for detection of apoptotic cells by terminal deoxynucleotidyl transferase-mediated dUTP-biotin nick-end labeling (TUNEL) assays in A4, SNA, SLA, and AR cells at steady state and on γ-irradiation (20 Gy for 36 hours; panels **(i), (ii), (iii),** and **(iv)** represent TUNEL staining, phase contrast, nuclear staining by PI, and merged images, respectively). Scale bars represent 50μ. **(E):** In vitro clonogenicity assay of steady-state (A4, SNA, SLA, AR, ASNsi, and ASLsi) and postirradiated (A4i, SNAi, SLAi, ARi, ASNsi-ir, and ASLsi-ir) cells. Representative graph shown for experiments done in triplicate; $p \leq .05$. Abbreviations: A4i, A4 cells exposed to γ-irradiation; AR, radioresistant A4 cells; ARi, AR cells exposed to γ-irradiation; ASLsi, A4 cells transfected with Slug; ASLsi-ir, postirradiated ASLsi cells; ASNsi, A4 cells transfected with Snail; ASNsi-ir, postirradiated ASNsi cells; FITC, fluorescein isothiocyanate; SLA, stable transfectants of A4 cells overexpressing Slug; SLAi, SLA cells exposed to γ-irradiation; SNA, stable transfectants of A4 cells overexpressing Snail; SNAi, SNA cells exposed to γ-irradiation.

cells correlated with an increased clonogenicity compared with parental A4 cells, exposure to irradiation drastically decreased this potential in A4 cells, although SNA, SLA, and AR cells continue to form colonies in soft agar, indicating a capacity for re-entry into cell cycle, cell survival, proliferation, and retention of tumorigenic capabilities (Fig. 3E).

We then sought to determine whether decreased levels of these TFs would reverse the above effects. Knocking out individual expression by transfecting parental A4 cells with either Snail or Slug siRNA (to generate ASNsi and ASLsi cells, respectively) indicated a distinct shift of the G0/G1 cell population toward sub-G0 phase in postirradiated ASNsi as well as ASLsi cells (ASNsi-ir and ASLsi-ir cells, respectively; Fig. 3B). This sub-G0 fraction was higher in Slug knockdown (50%) than in Snail knockdown (30%) cells, hinting possibly at a more protective role of Slug. Clonogenicity assays further indicated that silencing of either TF resulted in lower colony-formation efficiencies than that of scrambled sequence transfected A4 cells; furthermore, this capacity was almost completely abrogated after irradiation when either TF was silenced (Fig. 3E). Together our observations support a definitive correlation of the two TFs with radioresistance, since cells that express elevated levels of Snail and Slug are more capable of overcoming cell cycle arrest at the G2/M checkpoint to continue cycling, thereby effecting cell survival.

Chemoresistance of Ovarian Cancer Cells Is Also Associated with Upregulated Snail and Slug Levels

Toward exploring the possible involvement of Snail and Slug in chemoresistance—a serious concern in ovarian cancer, we developed A4 cells resistant to 5 nM paclitaxel (AC cells). These cells are spindle shaped and, like the AR clones, acquire a native overexpression of the two TFs during development of chemoresistance (supporting information Figs. 3, 6A). On exposure of parental A4, AC, SNA, and SLA to the LD50 dose of paclitaxel (0.7 nM, supporting information Fig. 2C; supporting information text), increased Snail and Slug mRNA and protein levels were evident in the treated cells (A4-px) compared with A4 and SNA, but not to the same extent in the treated AC, SLA, and SNA cells (AC-px, SLA-px, and SNA-px, respectively; supporting information Fig.

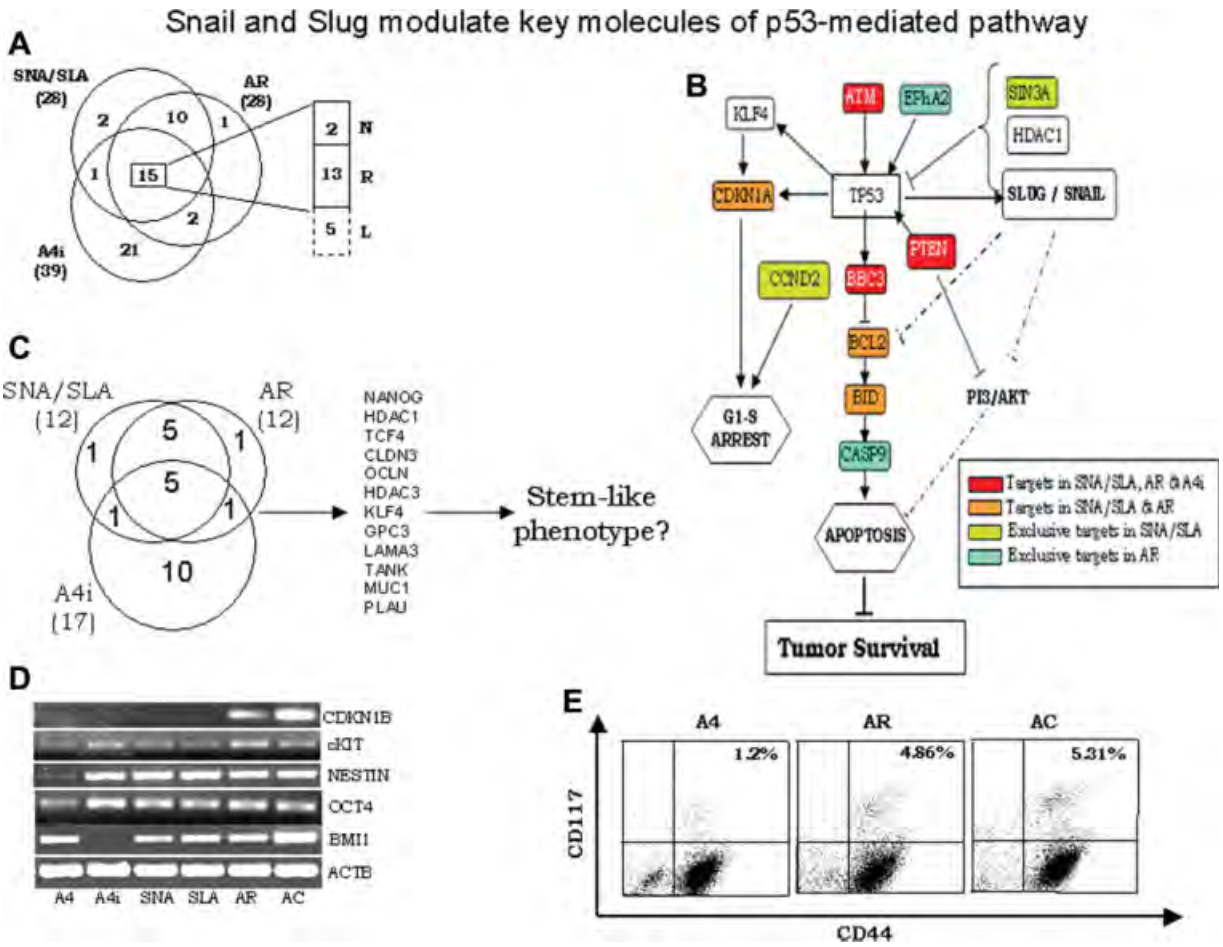

Figure 4. Ectopic or natively upregulated levels of Snail and Slug repress key molecules in p53-mediated apoptosis. **(A):** Venn diagram representing the overlap of gene targets in SNA/SLA (ectopic) and A4i, AR (native) cells upregulating Snail and Slug. Intercepting values indicate the common genes between the respective cell types. Of the 15 genes that were common to all cells, 2 were novel (N), 13 were retained (R), and 5 were lost (L) compared with the parental A4 cells. **(B):** Schematic representation indicating genes in p53-mediated DNA damage response pathway targeted by Snail and Slug in our study. **(C):** Venn diagram representing the overlap of gene targets that are lost in SNA/SLA (ectopic) and A4i and AR (native) cells upregulating Snail and Slug compared with parental A4 cells. Intercepting areas indicate numbers of common genes lost as targets—also included in the list. **(D):** Expression levels of stem cell markers in A4i, SNA, SLA, AR, and AC cells having enhanced expression of Snail and Slug compared with parental A4 cells. ACTB was used as an internal control. **(E):** Representative dot blot of CD44 and CD117 (c-kit) expression in AR and AC cells compared with parental A4 cells. Abbreviations: A4i, A4 cells exposed to γ-irradiation; AC, paclitaxel-resistant A4 cells; AR, radioresistant A4 cells; L, lost; N, novel; R, retained; SLA, stable transfectants of A4 cells overexpressing Slug; SNA, stable transfectants of A4 cells overexpressing Snail.

6B, 6C), which already express higher levels at steady state. Cell cycle analyses of these cells indicated significant apoptosis and G2-M arrest in A4-Px cells compared with parental A4 cells. However cell cycle profiles were not altered to the same extent in AC cells (supporting information Fig. 6D). Annexin V staining of these two cell types further confirmed the above findings (supporting information Fig. 6E).

Ectopic Overexpression and Native Upregulation of Snail and Slug Affects Specific Pathways

A striking observation was of the similarity between cellular states wherein Snail and Slug are upregulated vis-à-vis ectopic expression (SNA/SLA cells) and native upregulation (irradiated [A4i] and radioresistant [AR] cells), with respect to new targets acquired, retained, or lost over parental A4 cells. Moreover, the degree of this overlap was higher between the SNA, SLA, and AR cells than with the A4i cells; this correlates with higher postirradiation survival in the former three cell types as described earlier (Fig. 3). From the genes modulated in these states, we derived a consolidated overlap of 15 gene targets (Fig. 4A), of which two were novel targets (*BBC3/PUMA* and *MAPK3*), whereas 13 were retained from the parental A4 cells (*ATM*, *BRCA2*, *CDH1*, *PTEN*, etc.; supporting information Table 5). The 15 genes repressed by Snail and Slug under stress are suggested to be involved in mediating inhibition of either p53, p53 feedback loop 2, or EGF receptor signaling pathways (identified through pathway analyses using the gene expression analysis tool PANTHER; supporting information Fig. 7). Three of these 15 genes, namely ATM, *PTEN*, and *BBC3/PUMA*, were components of the p53 feedback loop 2; additional components of p53 signaling include *KLF4*, *CDKN1A*, *BCL2*, *BID*, *EPHA2*, and *CASP9* in SNA/SLA and/or AR cells (supporting information Fig. 8). The repression was validated and a good correlation between promoter occupancy of *BBC3*, *EPHA2*, and *BCL2* by Snail/Slug with their repression at the mRNA and protein levels was observed (supporting information Fig. 8); whereas similar promoter occupancy of *PTEN*, *ATM*, *CCND2*, *SIN3A*, and *CASP9* correlated with gene repression at the transcript level

(supporting information Fig. 9A). Thus, repression of various components of the p53 pathway by Snail and Slug under conditions of stress may mediate resistance to apoptosis.

Gene Targets Lost Through Natively Upregulated Snail and Slug Levels May Influence "Stemness"

NANOG, *HDAC1*, *CLDN3*, *OCLDN*, and *TCF4* were identified as possibly being derepressed through reduced promoter occupancy of Snail and Slug in cells that upregulate level(s) of these TFs, namely A4i/SNA/SLA/AR cells (supporting information Table 5). Additionally, *HDAC3*, *KLF4*, *GPC3*, *LAMA3*, *TANK*, *MUC1*, and *PLAU* were also lost as targets in at least two of these cell types (Fig. 4C; supporting information Table 6). We reasoned that such a derepression could indicate a definitive advantage for a cancer cell under stress. By virtue of its being a master transcriptional regulator for maintenance of undifferentiated stem cells [29], derepression of *NANOG*, *HDAC1*, and *HDAC3*, complemented by re-expression of KLF4 (associated with acquisition of pluripotency), suggests a mechanism for the acquisition of stem-like characteristics by these cells toward resisting genotoxicity. Good correlation of loss in promoter occupancy was evident with the re-expression of *NANOG*, *HDAC1*, *HDAC3*, *KLF4*, *CLDN3*, and *TCF4* at the transcript level (supporting information Fig. 9B). As further confirmation of association of derepression of a selective subset of genes with acquisition of stem-like characteristics, we probed A4, A4i, SNA, SLA, AR, and AC cells for the expression of additional stem cell markers. This profiling revealed a distinct upregulation of OCT4, NESTIN, and c-KIT (CD117); BMI-1, however, was markedly absent in the A4i cells (which have low levels of Nanog expression and cell survival); whereas the quiescence marker *CDKN1B* was expressed only in the AR and AC cells (Fig. 4D). The differential effects may be attributed to achievement of optimal dosage and cooperative effects of both TFs through a native upregulation during acquisition of radioresistance or chemoresistance. We further probed the three cell types, namely parental A4, AR, and AC cells, for expression of the surface phenotype $CD44^{+}/CD117^{+}$ that has been recently reported for ovarian cancer stem cells [30]. A fourfold to fivefold increase in the putative stem cell populations was evident in both the resistant cell types (Fig. 4E). The derepression of key molecules by Snail and Slug on exposure to stress, and their contribution to acquisition of resistance, thus appears to be one of the key contributory mechanisms in ovarian cancer resistance.

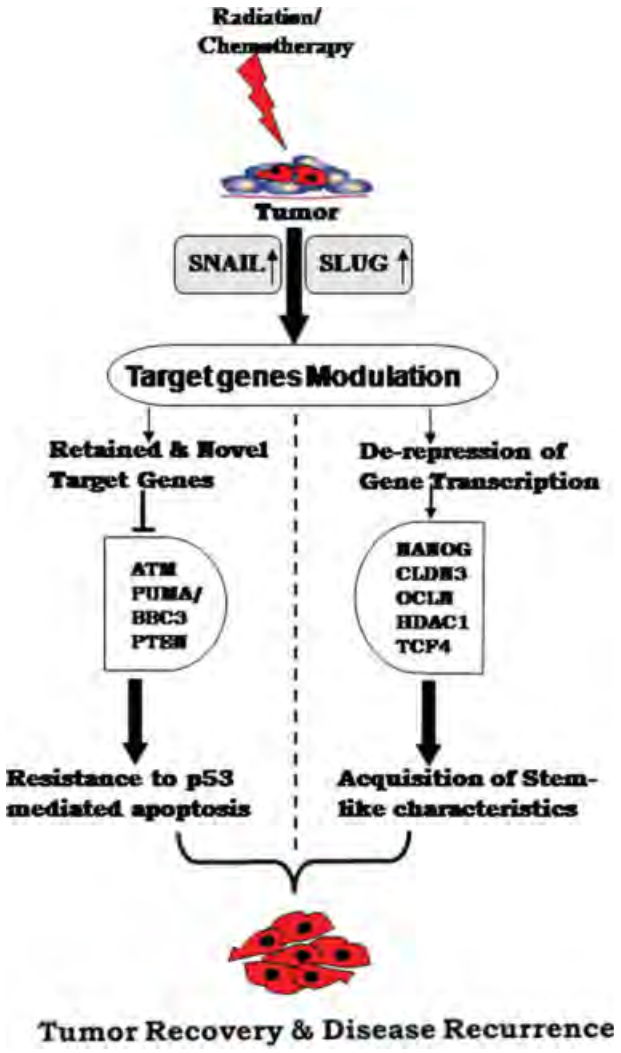

Figure 5. Model summarizing the mechanism of action of Snail and Slug in ovarian cancer cells exposed to stress. Snail and Slug expression is trigged in response to radiation and chemotherapy. These molecules perform two diverse effects, namely (a) repression of genes involved in p53-mediated apoptosis, which leads to enhanced cell survival, and (b) derepression of self-renewal genes, which leads to the acquisition of a stem cell-like phenotype. The outcome of these effects is failure of therapy, tumor cell recovery, and disease recurrence.

Discussion

In the present study, we report the upregulation of the transcriptional repressors Snail and Slug under conditions of radio-/drug-induced stress to modulate at least 47 genes in ovarian cancer (supporting information Fig. 10). Although this number of genes is likely to be a gross underrepresentation of the total repertoire of Snail and Slug targets, it extends the current understanding of their biological functionality in cancer. Through identification of this definitive modulation, we realized that Snail and Slug regulate at least two programs besides EMT in a cancer cell (Fig. 5):

(a). Direct participation of Snail and Slug in p53-mediated pro-survival signaling through active repression of pro-apoptotic genes *PUMA*/*BBC3*, *ATM* and *PTEN*. The transcription factor p53, activated by cellular stress, is reported to involve transactivation of Slug for partnering in its decision to arrest, repair, and mediate cell survival under stress [31, 32]. Slug represses *PUMA*/*BBC3*, a potent proapoptotic molecule [33], and is associated with radiosensitivity of stem cells [10, 11, 34, 35] and cisplatin sensitivity in ovarian cancer cells [36]. The role of Snail and Slug identified in the present study provides a mechanistic understanding of repression of *PUMA* that, although being in concordance with previous reports of Slug-mediated radioresistance of hematopoietic stem cells, appears to additionally involve inactivation of other components of the p53-mediated apoptotic pathway in the context of cancer including *ATM* and *Pten*.

(b). Snail and Slug regulate indirect/passive activation of a self-renewal program through loss of binding to specific gene promoters including *NANOG*, *HDAC1*, *TCF4*, *KLF4*, *HDAC3*, *GPC3*, and so on that were earlier repressed under steady-state conditions. On examining this gene modulation, we realized that the stemness program thus

activated by Snail and Slug further involves expression of other "stem cell markers," including Oct4, Bmi1, and nestin, and a fourfold/fivefold increase in the number of $CD44^{+}CD117^{+}$ cells (representative of ovarian CSCs [30]). The derepression is strongly suggestive of de novo generation of CSCs through dedifferentiation of cancer cells; it is also highly unlikely that indigenous CSCs would proliferate rapidly under conditions of stress to generate the enhanced numbers of resistant cells reported in minimal residual disease [37]. Therefore, our findings provide a mechanistic understanding for reports on enrichment of stem cells in tumors after therapy [38], as does the recent report linking EMT with generation of CSCs [5].

It has been proposed that only a subset of primary tumor cells with a distinct immunophenotype that involves several stem cell markers (e.g., expression of homing molecules: CXCR4 [39], aldehyde dehydrogenase [40], etc.) has the capability to metastasize [41]. Our findings extend this understanding to suggest that stem-like cells generated through activation of Snail and Slug, and bestowed with three critical capabilities, namely EMT, resistance to p53-mediated apoptosis, and a self-renewal program, actually define the functionality and survival of metastatic CSCs. EMT provides a mechanism of escape to a new, less adverse niche; resistance to apoptosis ensures cell survival in conditions of stress in the primary tumor; whereas acquisition of stemness characteristics ensures generation of the critical tumor mass required for progression of micrometastases to macrometastases.

Conclusions

The term "stem cell" was coined in the context of colony-forming cells surviving radiation and repopulating the spleen [42]; this defining capability to bide environmental stress is a necessity in the normal niches wherein stem cells perform tissue regenerative functions throughout the life span of an organism. Identification of stem cells in cancer was immediately realized to have a more important repercussion vis-à-vis recalcitrance of tumors to therapy and occurrence of minimal residual disease [36, 37, 43]. However, the mechanism underlying the enrichment of stem-like cells after treatment has never been resolved.

In the present work, we report a probable model of the involvement of transcription factors Snail and Slug and an elegant modulation of their targets under conditions of stress that effectively mediates cell survival and involves the acquisition of stem-like characteristics to ovarian cancer cells. This identification not only provides mechanistic understanding of the enrichment of stem cells in posttreatment tumors, but furthermore, our data hint that the de novo generation of CSCs by Snail and Slug probably represents directed dedifferentiation of cells in tumors since it is highly unlikely that CSCs would continue to self-renew/proliferate under conditions of stress to generate the enhanced numbers of resistant cells. Although the precise molecular intricacies of these effects in a recalcitrant tumor could be more complex and involve cooperative functioning of other molecules and could partly be related to continued evolution of resistance [44], our findings definitely suggest that Snail and Slug are critical determinants of disease progression. Although we have focused on these phenomena in ovarian cancer, our findings are possibly extendable to other cancers to represent a common, yet underestimated, mechanism that could make cancer cells difficult to eradicate.

Acknowledgments

We thank Dr. G.C. Mishra, Director, NCCS (Pune, India), for encouragement and support, and Prof. B.A. Chopade, Director, Institute of Bioinformatics and Biotechnology, for support and cooperation. Research is funded by the Department of Biotechnology, Government of India, New Delhi. N.K.K. received a research fellowship from the Council of Scientific and Industrial Research, New Delhi. We extend our gratitude to Prof. A. Cano for providing mSnail and mSlug constructs. Technical assistance by Mr. Avinash Mali, and the FACS and Confocal facilities at NCCS are gratefully acknowledged.

Disclosure of Potential Conflicts of Interest

The authors indicate no potential conflicts of interest.

References

1 Hanahan D, Weinberg RA. The hallmarks of cancer. Cell 2000;100:57–70.
2 Ito K, Bernardi R, Morotti A et al. PML targeting eradicates quiescent leukaemia-initiating cells. Nature 2008;453:1072–1078.
3 Bapat SA, Mali AM, Koppikar CB et al. Stem and progenitor-like cells contribute to the aggressive behavior of human epithelial ovarian cancer. Cancer Res 2005;65:3025–3029.
4 Sarrió D, Rodriguez-Pinilla SM, Hardisson D et al. Epithelial-mesenchymal transition in breast cancer relates to the basal-like phenotype. Cancer Res 2008;68:989–997.
5 Mani SA, Guo W, Liao MJ et al. The epithelial-mesenchymal transition generates cells with properties of stem cells. Cell 2008;133:704–715.
6 Morel AP, Lievre M, Thomas C et al. Generation of breast cancer stem cells through epithelial-mesenchymal transition. Plos One 2008;3:e2888.
7 Hemavathy K, Ashraf SI, Ip YT. Snail/Slug family of repressors: slowly going into the fast lane of development and cancer. Gene 2000;257:1–12.
8 Nieto MA. The snail superfamily of zinc-finger transcription factors. Nat Rev Mol Cell Biol 2002;3:155–166.
9 Baum B, Settleman J, Quinlan MP. Transitions between epithelial and mesenchymal states in development and disease. Semin Cell Dev Biol 2008;19:294–308.
10 Inoue A, Seidel MG, Wu W, Kamizono S et al. Slug, a highly conserved zinc finger transcriptional repressor, protects hematopoietic progenitor cells from radiation-induced apoptosis in vivo. Cancer Cell 2002;2:279–288.
11 Pérez-Losada J, Sanchez-Martin M, Perez-Caro M et al. The radioresistance biological function of the SCF/kit signaling pathway is mediated by the zinc-finger transcription factor Slug. Oncogene 2003;22:4205–4211.
12 Pérez-Caro M, Bermejo-Rodriguez C, Gonzalez-Herrero I et al. Transcriptomal profiling of the cellular response to DNA damage mediated by Slug (Snai2) Br J Cancer 2008;98:480–488.
13 Kurrey NK, Amit K, Bapat SA. Snail and Slug are major determinants of ovarian cancer invasiveness at the transcription level. Gynecol Oncol 2005;97:155–165.
14 Olmeda D, Moreno-Bueno G, Flores JM et al. SNAI1 is required for tumor growth and lymph node metastasis of human breast carcinoma MDA-MB-231 cells. Cancer Res 2007;67:11721–11731.
15 Hotz B, Arndt M, Dullat S. Epithelial to mesenchymal transition: expression of the regulators snail, slug, and twist in pancreatic cancer. Clin Cancer Res 2007;13:4769–4776.
16 Barrallo-Gimeno A, Nieto MA. The Snail genes as inducers of cell movement and survival: implications in development and cancer. Development 2005;132:3151–3161.

17 Ahmed N, Thompson EW, Quinn MA. Epithelial-mesenchymal interconversions in normal ovarian surface epithelium and ovarian carcinomas: an exception to the norm. J Cell Physiol 2007;213: 581–588.
18 Brabletz S, Schmalhofer O, Brabletz T. Gastrointestinal stem cells in development cancer. J Pathol 2009;217:307–317.
19 Batlle E, Sancho E, Franci C et al. The transcription factor snail is a repressor of E-cadherin gene expression in epithelial tumour cells. Nat Cell Biol 2000;2:84–89.
20 Cano A, Perez-Moreno MA, Rodrigo I et al. The transcription factor snail controls epithelial-mesenchymal transitions by repressing E-cadherin expression. Nat Cell Biol 2000;2:76–83.
21 Peinado H, Ballestar E, Esteller M et al. Snail mediates E-cadherin repression by the recruitment of the Sin3A/histone deacetylase 1 (HDAC1)/HDAC2 complex. Mol Cell Biol 2004;24:306–319.
22 Boyer LA, Lee TI, Cole MF et al. Core transcriptional regulatory circuitry in human embryonic stem cells. Cell 2005;122:947–956.
23 Barrett T, Troup DB, Wilhite SE et al. NCBI GEO: mining tens of millions of expression profiles–database and tools update. Nucleic Acids Res 2007;35:D760–D765.
24 Moreno-Bueno G, Cubillo E, Sarrio D et al. Genetic profiling of epithelial cells expressing E-cadherin repressors reveals a distinct role for Snail, Slug, And E47 Factors In epithelial-mesenchymal Transition Cancer Res 2006;66:9543–9556.
25 De Craene B, Gilbert B, Stove C et al. The transcription factor snail induces tumor cell invasion through modulation of the epithelial cell differentiation program. Cancer Res 2005;65:6237–6244.
26 Zeitlinger J, Zinzen RP, Stark A et al. Whole-genome ChIP-chip analysis of Dorsal, Twist, and Snail suggests integration of diverse patterning processes in the Drosophila embryo. Genes Dev 2007;21: 385–390.
27 Birney E, Stamatoyannopoulos JA, Dutta A et al. Identification and analysis of functional elements in 1% of the human genome by the ENCODE pilot project. Nature 2007;447:799–816.
28 Guaita S, Puig I, Franci C et al. Snail induction of epithelial to mesenchymal transition in tumor cells is accompanied by MUC1 repression and ZEB1 expression. J Biol Chem 2002;277:39209–39216.
29 Torres J, Watt FM. Nanog maintains pluripotency of mouse embryonic stem cells by inhibiting NFkappaB and cooperating with Stat3. Nat Cell Biol 2008;10:194–201.
30 Zhang S, Balch C, Chan MW et al. Identification and characterization of ovarian cancer-initiating cells from primary human tumors. Cancer Res 2008;68:4311–4320.
31 Ferbeyre G, de Stanchina E, Lin AW et al. Oncogenic ras and p53 cooperate to induce cellular senescence. Mol Cell Biol 2002;22:3497–3508.
32 Seidel MG, Look AT. E2A-HLF usurps control of evolutionarily conserved survival pathways. Oncogene 2001;20:5718–5725.
33 Chipuk JE, Bouchier-Hayes L, Kuwana T et al. PUMA couples the nuclear and cytoplasmic proapoptotic function of p53. Science 2005; 309:1732–1735.
34 Wu WS, Heinrichs S, Xu D et al. Slug antagonizes p53-mediated apoptosis of hematopoietic progenitors by repressing puma. Cell 2005; 123:641–653.
35 Qiu W, Carson-Walter EB, Liu H et al. PUMA regulates intestinal progenitor cell radiosensitivity and gastrointestinal syndrome. Cell Stem Cell 2008;2:576–583.
36 Fraser M, Bai T, Tsang BK. Akt promotes cisplatin resistance in human ovarian cancer cells through inhibition of p53 phosphorylation and nuclear function. Int J Cancer 2008;122:534–546.
37 Eyler CE, Rich JN. Survival of the fittest: Cancer stem cells in therapeutic resistance and angiogenesis. J Clin Oncol 2008;26:2839–2845.
38 Baumann M, Krause M, Hill R. Exploring the role of cancer stem cells in radioresistance. Nat Rev Cancer 2008;8:545–554.
39 Hermann PC, Huber SL, Herrler T et al. Distinct populations of cancer stem cells determine tumor growth and metastatic activity in human pancreatic cancer. Cell Stem Cell 2007;1:313–323.
40 Croker AK, Goodale D, Chu J et al. High aldehyde dehydrogenase and expression of cancer stem cell markers selects for breast cancer cells with enhanced malignant and metastatic ability. J Cell Mol Med 2008 [Epub ahead of print].
41 Jung A, Brabletz T, Kirchner T. The migrating cancer stem cells model–a conceptual explanation of malignant tumour progression. Ernst Schering Found Symp Proc 2006;109–124.
42 Till JE, Mcculloch EA, Siminovitch L. A stochastic model of stem cell proliferation, based on the growth of spleen colony-forming cells. Proc Natl Acad Sci U S A 1964;51:29–36.
43 Ajani JA, Izzo JG, Lee JS. Chemotherapy and radiotherapy resistance: complexity, reality, and promise. J Clin Oncol 2009;27:162–163.
44 Boman BM, Wicha MS. Cancer stem cells: A step towards the Cure. J Clin Oncol 2008;26:2795–2799.


See www.StemCells.com for supporting information available online.

Carcinogenesis, 2020, Vol. 41, No. 4, 515–526

doi:10.1093/carcin/bgz119
Advance Access Publication June 25, 2019
Original Article

ORIGINAL ARTICLE

Functional balance between Tcf21–Slug defines cellular plasticity and migratory modalities in high grade serous ovarian cancer cell lines

Sagar S.Varankar, Madhuri More, Ancy Abraham, Kshama Pansare[1], Brijesh Kumar, Nivedhitha J.Narayanan, Mohit Kumar Jolly[2,3], Avinash M.Mali and Sharmila A.Bapat[*]

National Centre for Cell Science, Savitribai Phule Pune University, Ganeshkhind, Pune 411007, India, [1]Institute for Plasma Research & Tata Memorial Centre, Kharghar, Navi-Mumbai, India and [2]Center for Theoretical Biological Physics, Rice University, Houston, TX, USA [3]Present addresses: Centre for Biosystems Science and Engineering, Indian Institute of Science, Bangalore 560012, India.

[*]To whom correspondence should be addressed. Tel: +91 020 25708089; Fax: +91 20 25692259; Email: sabapat@nccs.res.in

Abstract

Cellular plasticity and transitional phenotypes add to complexities of cancer metastasis that can be initiated by single cell epithelial to mesenchymal transition (EMT) or cooperative cell migration (CCM). Our study identifies novel regulatory cross-talks between Tcf21 and Slug in mediating phenotypic and migration plasticity in high-grade serous ovarian adenocarcinoma (HGSC). Differential expression and subcellular localization associate Tcf21, Slug with epithelial, mesenchymal phenotypes, respectively; however, gene manipulation approaches identify their association with additional intermediate phenotypic states, implying the existence of a multistep epithelial-mesenchymal transition program. Live imaging further associated distinct migratory modalities with the Tcf21/Slug status of cell systems and discerned proliferative/passive CCM, active CCM and EMT modes of migration. Tcf21–Slug balance identified across a phenotypic spectrum in HGSC cell lines, associated with microenvironment-induced transitions and the emergence of an epithelial phenotype following drug exposure. Phenotypic transitions and associated functionalities following drug exposure were affirmed to ensue from occupancy of Slug promoter E-box sequences by Tcf21. Our study effectively provides a framework for understanding the relevance of ovarian cancer plasticity as a function of two transcription factors.

Introduction

Intrinsic cellular identities originate during embryonic commitment and are fated for tissue specific spatiotemporal roles through cross-talks with niche components (1). Destabilization of homeostasis under pathological conditions alters the tissue milieu to revoke inherent cellular plasticity and restore primitive phenotype(s), architecture and functions to facilitate disease progression (2,3). Cooperative action of regulatory molecular circuits such as the role of Slug–Sox9 in maintenance of mammary basal and luminal epithelial cells, are diverted in aberrant contexts like cell transformation to redefine cell fates (4,5). Innate capabilities and perturbed microenvironment thus align as distinct etiologies in cancer (6,7). Previous studies in epithelial ovarian carcinomas (EOC) identified Stem-A, Stem-B, Epi-A, Epi-B and Mes subtypes that correspond with epithelial (E), intermediate epithelial (iE), intermediate mesenchymal (iM) and mesenchymal (M) phenotypic features (8,9); a subsequent study reported iE and iM as extensions of an epithelial-mesenchymal hybrid state (EM). Furthermore, comprehensive analyses of the most aggressive EOC *viz.* high-grade serous adenocarcinomas (HGSC) have revealed diverse molecular signatures that

Received: February 22, 2019; **Revised:** April 26, 2019; **Accepted:** June 21, 2019

Abbreviations

aCCM active collective cell migration
BMP7 bone morphogenetic protein 7
CCM cooperative cell migration
Cdh1 E-cadherin
E epithelial
EM epithelial-mesenchymal hybrid
EMT epithelial to mesenchymal transition
HGSC high grade serous carcinoma
iE intermediate epithelial
iM intermediate mesenchymal
K/O knock-out
M mesenchymal
Nn nearest neighbors
OE overexpression
pCCM passive collective cell migration
SS serum starved
TCGA The Cancer Genome Atlas
TF transcription factors
TGFβ transforming growth factor β
Vim vimentin

correlate with epithelial/differentiated (E/D), mesenchymal (M), proliferative (P), immunoreactive (IR) features and require adoption of differential therapeutic strategies (10–13). Hence, the disparate collation of EOC datasets can misrepresent the clinical associations of tumor subtypes with phenotypic states and should be avoided to improve disease management.

Our previous analyses of HGSC expression datasets in The Cancer Genome Atlas (TCGA) resolved three molecular subclasses associated with discrete mechanisms of metastases. Class 1 exhibited cooperative cell migration (CCM), Class 2 associated with epithelial-mesenchymal transitions (EMT) while Class 3 presented with mixed features (11,14). Correlating with reports using the same datasets suggested CCM-Class tumors to present as P/D/iE subclass, EMT-Class tumors as M/IR/iM while the heterogeneous Class 3 tumors possibly represent IR/D phenotypes. While molecular signatures for HGSC subtypes have been defined across multiple studies, the limited comprehension of aberrantly activated plasticity programs curb effective translation of previous findings. In the present study, we discern HGSC cell phenotypes (E/M/intermediates) as a function of Tcf21 and Slug expression, localization and activity. Functional evaluation assisted by real-time imaging, associated phenotypic states with either EMT, active CCM or proliferative (annotated as passive CCM/pCCM) modes of wound closure. As opposed to the rigidity of epithelial/mesenchymal phenotypes, intermediate states exhibited transitions between EMT and, active collective cell migration (aCCM) (but not pCCM) modalities and responded with enhanced plasticity in presence of positive/negative growth regulators as a function of altered Tcf21–Slug subcellular localization. Strikingly, emergence of epithelial features involved transcriptional repression of Slug by Tcf21. Our study thus, highlights the antagonistic interplay of Tcf21–Slug in maintenance of distinct cellular phenotypes and presents them as potential biomarkers for phenotype-assisted tumor stratification.

Materials and methods

Cell culture

Ovarian cancer cell lines used in the study were all of the high grade serous histology (15,16). A4 cells were previously established in our lab from ascites of a HGSC patient (17), OVCAR3 cells were obtained from the cell repository at NCCS, Pune, India. Dr S. Mok (M. D. Anderson Cancer Center, TX) and Prof. Viktor Magdalen (Klinische Forschergruppe der Frauenklinik der TU München) provided OV90 and OVMZ6 cell lines, respectively. OVCA420, PEO14, OVCA432 and CAOV3 cells were provided by Prof. Judith Clements (Translational Research Institute, Australia). OVCAR3, OVCA432, CAOV3, OV90, OVCA420 and PEO14 cells were grown in RPMI 1640 (Gibco, Waltham, MA) supplemented with 10% fetal bovine serum. A4 cells were cultured in Minimal Essential Medium/MEM (Gibco) supplemented with 5% fetal bovine serum and 1% nonessential amino acids; Dulbecco's Modified Essential Medium/DMEM (Gibco) supplemented with 5% serum, 100 μM asparagine (Sigma, St. Louis, MO) and 100 μM arginine (Sigma) was used for culturing OVMZ6 cells. All cell lines were maintained in a humidified incubator at 37°C under a 5% CO_2 atmosphere. Cell lines were authenticated by short tandem repeat profiling and comparison with ATCC and EACC databases (June 2018).

Transfection, generation of TF derivative clones

For generation of knockouts via genomic editing OVCAR3 and A4 cells were transfected with 500 ng of commercially available CrispR_GFP vectors against Tcf21 and Slug (Sigma), respectively using Lipofectamine 3000 (Invitrogen, Carlsbad, CA) as per the manufacturer's protocol. Post transfection, cells were incubated at 30°C for 48 h to ensure optimal CrispR activity that was confirmed by the T7 endonuclease assay (data not provided). Single cell sorting of GFP positive cells was performed with BD Aria II SORP into 96 well plates. Sorted cells were allowed to grow for clone establishment and subjected to molecular (qPCR, immunoblotting, immunofluorescence staining) and functional (*in vitro* wound closure) validation. Successful knockouts (E2–Tcf21 knockout, D7–Slug knockout) obtained from CrispR transfections, were further transfected with GFP vectors for Slug and Tcf21, respectively, sorted to obtain single cell clones and validated. $Tcf21^{K/O}Slug^{OE}$ clones could not be established due to rapid apoptosis.

Treatments

Cells were treated as follows before RNA extraction and immunofluorescence staining:
Serum deprivation: cells were allowed to grow for 24 h post-seeding, following which spent medium for each cell line was replaced with equal volume of serum free media as indicated for each cell line. *Growth factor exposure:* 24 h following serum deprivation, cell lines were exposed to either bone morphogenetic protein 7 (BMP7) (10 ng/ml), TGFβ (10 ng/ml) or a combination of both (Invitrogen). *Paclitaxel treatment:* cells were allowed to grow for 24 h post-seeding, after which spent medium for each cell line was replaced with equal volume of complete medium containing IC50 concentrations of paclitaxel (Sigma) optimized for each cell line (IC50 values for each cell line are available on request). 0.1% DMSO was used as a vehicle control.

Derivation of TF network, correlation and expression analysis of TFs and phenotypic markers in TCGA–HGSC dataset

Details are provided in Supplementary Material, available at *Carcinogenesis* Online.

RNA extraction, cDNA synthesis, RT-PCR and qPCR

Trizol (Invitrogen) based total RNA extraction was achieved from 80% confluent cultures of cell lines following respective treatments as described previously (18). Details are provided in Supplementary Material, available at *Carcinogenesis* Online along with list of primers.

Immunostaining, image acquisition and quantification of signal intensity

Immunostaining was performed as described previously (18). Quantification of signal intensities for transcription factors was performed with the LAS-AF software (Leica Microsystems, Wetzlar, Germany). Briefly, ROIs were defined from phase contrast images around nuclear margins (for TFs) or cell boundaries (for E-cadherin [Cdh1], Vim) of each cell followed by extraction of signal intensities for Hoechst and respective

fluorescent channels. Relative nuclear signal intensity for transcription factors was determined as a ratio of TF-/Hoechst-associated fluorescence, while Cdh1,Vim were normalized to unstained (primary antibody control) samples to eliminate nonspecific signals obtained due to the staining protocol. Quantification was performed for a minimum of 50 nuclei for each sample. List of antibodies used is provided in Supplementary Material, available at *Carcinogenesis* Online.

Immunoblotting

Immunoblotting protocols were followed as described previously (18). List of antibodies used is provided in Supplementary Material, available at *Carcinogenesis* Online.

In vitro wound healing assay, live cell imaging, processing and quantification of data, principal component analysis for migration

Wound healing assay was performed as per previous protocols (14). Under specific experimental conditions media additives were administered including 5% serum, TGFβ (10 ng/ml), BMP7 (10 ng/ml) or a combination of both growth factors. The wound was allowed to heal and was monitored up to 144 h. Images were captured on Olympus IX71 microscope and analyzed by the T-Scratch Software (Tobias Gebäck and Martin Schulz).

For live cell imaging, images were acquired for 30 h, following infliction of wound on a cell monolayer, on an inverted laser scanning confocal fluorescence LPSS5 microscope maintained at 37°C, 5% CO_2 atmosphere (Leica Microsystems). In case of specific treatments, additives were added as described previously. For live cell imaging of paclitaxel-treated cells, drug treatment for 48 h was followed by harvesting of residual cells and seeding for wound healing assay. In the absence of additives, live cell imaging was performed in serum free media in the presence of 20 ng/ml of mitomycin 'C' (Sigma). Images captured for live cell imaging were exported from the LAS AF software (Leica Microsystems) with .avi extensions. For elimination of shadow effects in images.avi files were opened in Fiji software, duplicated, inverted and averaged with original image using the Image Calculator. Processed files were subjected to thresholding to obtain binary images which were eventually processed through MTrack2 plugin to obtain X and Y coordinates for all the cells detected in the microscopic field of interest. Positional coordinates over a period of 16 h was used to calculate mean displacement and velocity for each cell, however, cells lacking this data at any time point were excluded from further analysis. Furthermore, binary images were processed through the BioVoxxel plugin to determine the mean number of nearest neighbors (Nn) around each cell particle. One cell diameter was used as a threshold to identify Nn around each cell as depicted in Supplementary Figure S2, available at *Carcinogenesis* Online. Mean displacement, velocity and number of Nn were analyzed in matlab2013b (Mathworks) with an open source code available for principal component analysis. First two components capturing maximum variance of the data were represented using SigmaPlot 10.0 software (SPSS).

Boyden chamber invasion assay

Trans-well invasion assays were performed, as described previously (19).

Suspension culture assessment

Suspension cultures for HGSC cell lines were generated as described by earlier studies (20).

FACS sorting and flow cytometry

FACS and Flow cytometry were performed as described previously (20). List of antibodies used is provided in Supplementary Material, available at *Carcinogenesis* Online.

Cloning, expression and purification of GST–Tcf21 protein

Human Tcf21 cDNA was amplified from A4 cells, cloned into pGEX-6P-1 GST vector and transformed into *Escherichia coli* BL21 codon Plus (Agilent Technologies, Santa Clara, CA). Details of cloning and protein purification are provided in Supplementary Materials and Methods, available at *Carcinogenesis* Online.

Electrophoretic mobility shift assay (EMSA)

EMSA was performed as described previously (18).

Chromatin immunoprecipitation assay and ChIP-PCR

ChIP was performed as described earlier (19); ChIPped DNA amplified using the GenomePlex Complete Whole Genome amplification kit as per manufacturer's instructions (Sigma). Specific primers were used to amplify E-boxes within promoter regions of genes, amplified products run on 1.5% agarose gels, and band intensities measured by densitometric analysis using Genetool3.6 (Syngene, Bengaluru, India). List of antibodies and primers used is provided in Supplementary Material, available at *Carcinogenesis* Online.

Luciferase constructs and luciferase assay

Luciferase constructs for E-cadherin and Slug wild-type promoters along with deletion mutants ΔS1–S2 were previously generated in the pGL3 luciferase plasmid (18). All constructs were verified by sequencing. 0.5 × 10^5 OVCAR3, A4, and derivatives were transfected with 0.5 μg luciferase reporter plasmids control and E-cadherin/Slug promoter containing plasmids in 24-well plates using Lipofectamine 3000 (Invitrogen). Renilla luciferase was added (10 ng) to each transfection as control. Luciferase activity was measured using a Dual Luciferase assay kit (Promega, Madison, WI) either post-transfection with pEGFP–Tcf21 and/or post paclitaxel treatment. Empty pEGFP and pGL3 vectors were used as controls.

Quantitative and statistical analysis

Pearson's correlation coefficient across the TCGA–HGSC datasets was calculated using the GraphPad Prism 6.0 software. Significant differences in gene expression profiles across the HGSC cell line panel were calculated by one-way analysis of variance using the Sigma Stat 3.5 Software. Significant differences following treatments in gene expression profiles, invasive capabilities and wound healing properties of HGSC cell lines and derivative clones, and luciferase activity for promoter assays were calculated by paired Student's *t*-test using the Sigma Stat 3.5 Software. Similarly, ChIP binding efficiencies were calculated by unpaired Student's *t*-test. Differences in nuclear intensities of Tcf21, Slug, Cdh1 and Vim were calculated by Tukey's test using the Sigma Stat 3.5 Software. Differences were considered significant if $P < 0.05$.

Results

Tcf21 and Slug expression governs a multistep phenotypic axis in HGSC

Previous data (14) identified class-specific expression of 13 transcription factors that were examined in the present study for association with distinct phenotypic states in HGSC (TFs; Supplementary Table S1, available at *Carcinogenesis* Online); immunomodulatory TFs AIF1, ETV7 were excluded from further analysis due to limitations of our experimental systems. Promoter occupancies between the remaining TFs, derived from consensus DNA binding sequences, predicted a cross-regulatory network that included 10 TFs from Class 1 (CCM/epithelial tumor class) *viz.*, *Tcf21*, *Sall2*, *Peg3*, *Gata4*, *Kcnip3*, *Znf219*, *Foxl2*, *Gli1*, *Sox12*, *Tcf7l1* and one TF *viz.*, Slug from Class 2 (EMT/mesenchymal tumor class; Figure 1a; Supplementary Figure S1a, available at *Carcinogenesis* Online; details of TF network generation are provided in Supplementary Material, available at *Carcinogenesis* Online) Correlation analysis among these TFs predicted coregulation of *Tcf21*, *Gata4*, *Peg3*, *Gli1*, *Foxl2* that correlated positively with each other and negatively

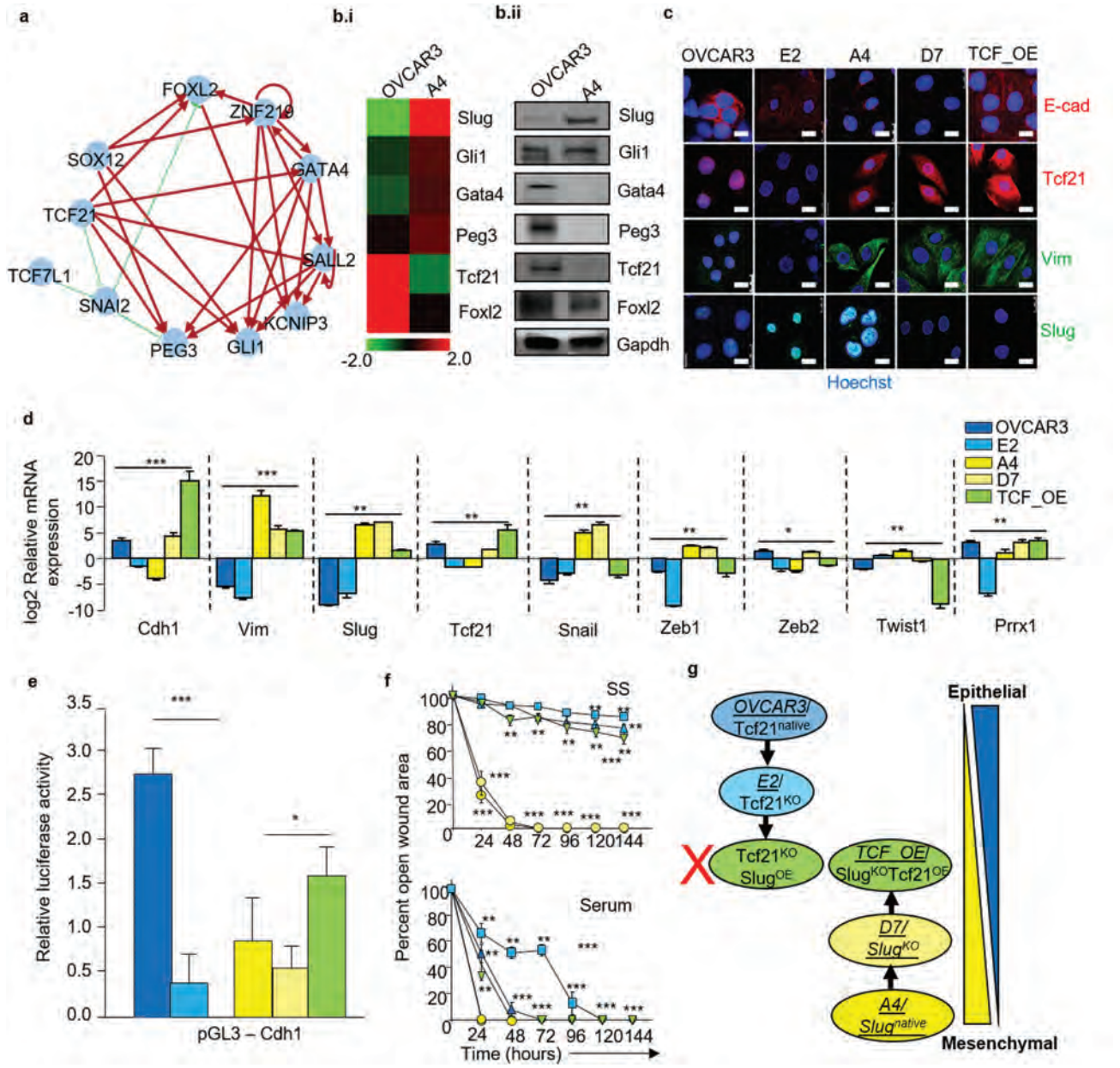

Figure 1. Tcf21 and Slug govern cellular phenotypes in HGSC. (**a**) Predicted transcription factor (TF) network of cross-regulatory activities, red arrows/green bars represent likely activator/repressor functions respectively; (**b**) Expression profiling of *Snai2*(Slug), *Gli1*, *Gata4*, *Peg3*, *Tcf21*, *Foxl2* in OVCAR3 and A4 cells by (i) qPCR (heatmap) and (ii) immunoblotting, GAPDH used as endogenous control. Immunoblots represented in the panel are derived from the same experiment and have been processed in parallel; (**c**) Immunostaining of Tcf21, Slug, Ecad, Vim in parental (OVCAR3/Tcf21^{native}, A4/Slug^{native}) and derivative cells (E2/Tcf21$^{K/O}$, D7/Slug$^{K/O}$ and TCF_OE/Slug$^{K/O}$Tcf21^{OE}), nuclei visualized with Hoechst, Scale bars—20 μm; (**d**) Expression profiles of phenotypic markers (*Cdh1*, *Vim*) and TFs (*Snai2*-Slug, *Tcf21*, *Snail*, *Zeb1*, *Zeb2*, *Twist1*, *Prrx1*) in parental (OVCAR3, A4) and derivative (E2, D7, TCF_OE) cells, normalization with GAPDH; (**e**) Reporter assays to determine the E-cadherin promoter activity in derivative clones (E2, D7, TCF_OE) and parental cells (OVCAR3, A4), luciferase activity normalized to native luciferase vector: pGL3; f. Graphical representation of wound healing efficiency of parental (OVCAR3, A4) and derivative cells (E2, D7, TCF_OE), in the absence and presence of serum (upper and lower panels respectively); (**g**) Flow chart depicting an epithelial–mesenchymal (EM) axis along which parental (OVCAR3, A4) and derivative cells (E2, D7, TCF_OE) are placed. Color scheme depicts each of the cell lines represented in preceding panels. All data are representative of experiments performed in triplicate and depicted as mean ± SEM. $^{*}P < 0.05$, $^{**}P < 0.01$, $^{***}P < 0.001$.

with *Snai2* (Slug) in the TCGA dataset (Supplementary Figure S1b, available at *Carcinogenesis* Online). Profiling these TFs in class-representative cell lines robustly associated CCM-Class (OVCAR3 cells) with Tcf21 and EMT-Class (A4 cells) with Slug expression; however, the lack of a strong correlation between mRNA and protein profiles limited their further validation (Figure 1b; Supplementary Figure S1c, available at *Carcinogenesis* Online). Thus, molecular profiles in our cell line models and previous association of Tcf21, Slug with the epithelial, mesenchymal phenotypes, respectively (19,21), prompted our focused efforts on discerning their role in cellular plasticity of ovarian cancer cell lines.

Toward ascertaining the role of Tcf21 and Slug in phenotype maintenance, we further derived knockout (K/O) clones of the dominant TF (genomic editing by commercial CrispR constructs) followed by overexpression (OE) of the other TF in parental cell

lines—OVCAR3 (Tcf21^{native}) and A4 (Slug^{native}; Supplementary Figure S1d, available at *Carcinogenesis* Online); stable knockouts were affirmed by sequencing (data not shown). Molecular profiles revealed high Tcf21, E-cadherin (*Cdh1*) expression in OVCAR3 cells whereas Tcf21$^{K/O}$(E2) exhibited high nuclear Slug and low *Cdh1*. A4 cells expressed high Slug, Vimentin (*Vim*) with low *Cdh1*, however, sustained expression of other EMT–TFs (Zeb1/2, Twist1, Snail, Prrx1) in the Slug$^{K/O}$ (D7) led to minimally altered *Cdh1* and *Vim* despite enhanced nuclear Tcf21 localization (Figures 1c and d). Interestingly, A4_Slug$^{K/O}$Tcf21^{OE} (TCF_OE) cells exhibited reduced expression of EMT–TFs and correlated with enhanced *Cdh1* while retaining *Vim* expression (Figures 1c and d). High luciferase activity in OVCAR3 and TCF_OE cells (reporter assay for *Cdh1* promoter harboring Slug binding E-box sequences), and reduced activity in E2, A4 and D7 cells suggested phenotypic variability as a function of Tcf21 and Slug expression (Figure 1e). Functional validation identified differential rates of wound closure between parental and derivative clones to be positively influenced by serum (Figure 1f). In the absence of serum, OVCAR3 and E2 cells failed to induce wound closure, suggesting the absence of functional EMT despite enhanced *Slug* and reduced *Cdh1* levels in E2 cells; wound healing efficacy was drastically curbed in TCF_OE as compared with A4 and D7 cells. Derivative clones, thus represented intermediate phenotypes along the EM axis wherein OVCAR3 (Tcf21^{native}) and E2 (Tcf21$^{K/O}$) exhibited a rigidity toward functional phenotypic alteration as compared with A4 (Slug^{native}), D7 (Slug$^{K/O}$) and TCF_OE (Slug$^{K/O}$Tcf21^{OE}) cells as indicated by molecular and functional readouts (Figure 1g). These findings while associating Tcf21, Slug with epithelial, mesenchymal phenotypes, respectively, highlight the inability of these TFs toward inducing a bilateral phenotypic switch and possibly imply EM transitions as a multistep process.

Tcf21–Slug status of HGSC cells associates with differential modes of migration

A disconnect between wound closure efficacies and expression of phenotypic markers in derivative clones prompted the adoption of high-resolution approaches to investigate their respective migratory modalities. Time lapse microscopy imaging improved the *in vitro* wound healing assay by enhancing the visual output. OVCAR3 and E2 cells exhibited proliferation-driven cell displacement that we termed passive CCM (pCCM), A4 mediated rapid wound healing through a combination of single cell and active CCM (EMT and aCCM, respectively) while its derivatives D7, (Slug$^{K/O}$Tcf21^{OE}) exhibited aCCM exclusively (Supplementary Video S1, available at *Carcinogenesis* Online). Cell position coordinates during wound closure allowed quantification of these processes by virtue of migration trajectories, mean cell velocity and Nn (Supplementary Figure S2, available at *Carcinogenesis* Online). pCCM driven wound closure was associated with minimal cell displacement, low migratory velocity and a high Nn; aCCM was defined by moderate displacement/velocity and high Nn while EMT cells exhibited high displacement/velocity with low Nn (Figure 2a–c). Serum addition enhanced displacement, velocity and reduced Nn in aCCM and EMT phenotypes while pCCM cells increased Nn by virtue of extensive cell proliferation. Presence of mitomycin 'C', a proliferation inhibitor, in the absence of serum distinguished cell displacement attributed by active migration (aCCM/EMT) as opposed to cell division driven passive movement (pCCM). Principal component analysis performed with these datasets supported differential migratory modes wherein PC1 (variance between velocity and displacement versus Nn) and PC2 (variance between displacement versus velocity) effectively resolved cell lines associated with pCCM, aCCM and EMT–aCCM modes of migration while capturing serum induced shifts in respective modalities (Figure 2d). Differential Nn frequencies between A4 and D7 proved a useful metric for distinguishing EMT from aCCM apart from the visualization in real time imaging. While visual outputs affirmed association of Tcf21 and Slug with distinct migratory modes in the derivative clones, principal component analysis permitted an unbiased segregation of these modalities as a function of TF expression. This gradient of migration modalities effectively agrees with the artificial E to M spectrum depicted in Figure 1g, emphasizing rigidity of the E phenotype, and supporting the absence of biphasic phenotypic switches in HGSC.

Tcf21 is a transcriptional repressor of Slug

In view of the predictive TF network and inverse associations in our derivative clones, we probed possible cross-regulation between Tcf21 and Slug. Luciferase activity (reporter assay for *SNAI2* promoter harboring Tcf21-binding consensus E-box sequences) was severely reduced in A4 cells exogenously overexpressing Tcf21 (Figure 3a and b). *In vitro* binding assays also affirmed physical interactions between recombinant Tcf21 and S1, S3, S5 *SNAI2* E-boxes. Further probing of Tcf21-bound chromatin complexes in OVCAR3 cells through immunoprecipitation indicated affinity for S2, S3, S6 *SNAI2* E-boxes (Figure 3c and d). Similar regulation of Tcf21 expression by Slug was not observed. Varied Tcf21 binding affinities in cell-free and cell-based systems emphasize the significance of cellular context in target recognition and imply possible involvement of other coregulatory factors in the process. These findings suggest transcriptional repression of Slug by Tcf21 toward maintenance of epithelial properties in HGSC.

HGSC tumors and cell lines intrinsically display a spectrum of phenotypes and modes of migration

Toward resolution of distinct phenotypes in HGSC at steady state and describing EM transitions as a multistep process, we primarily analyzed the heterogeneity of phenotypic markers in TCGA–HGSC dataset. Correlation analysis of gene expression data for epithelial and mesenchymal markers generated four clusters (C1–C4) representative of specific phenotypic attributes (Supplementary Figure S3a, available at *Carcinogenesis* Online). C1 genes included components of epithelial cell junctions and keratins, C2 genes associated with mesothelial and myoepithelial phenotypes across several tissues (breast, ovary, peritoneal linings) (22–24), C3 comprised of cell junction molecules encountered in mesenchymal cells (10), while C4 included genes commonly expressed in the endothelial and stromal lineages (25,26). Apart from segregation of these gene groups, correlation analysis identified a heterogeneity of phenotypic markers in HGSC which could be indicative of existing diverse phenotypes. Hierarchical clustering of known epithelial and mesenchymal TFs in this data yielded five distinct tumor groups (Supplementary Figure S3b, available at *Carcinogenesis* Online). Two of these were exclusively epithelial (E) and mesenchymal (M) while a third was considered EM by virtue of a heterogeneous double-positive signature. A separate cluster identified as intermediate E (iE), expressed E markers, Snail, Twist1 but lacked Tcf21, while the tumor group with low EMT–TF expression was assigned as iM.

In vitro validation of identified phenotypic states proceeded *via* parallel screening of E, M markers and TF transcripts across a panel of HGSC cell lines. Molecular profiles

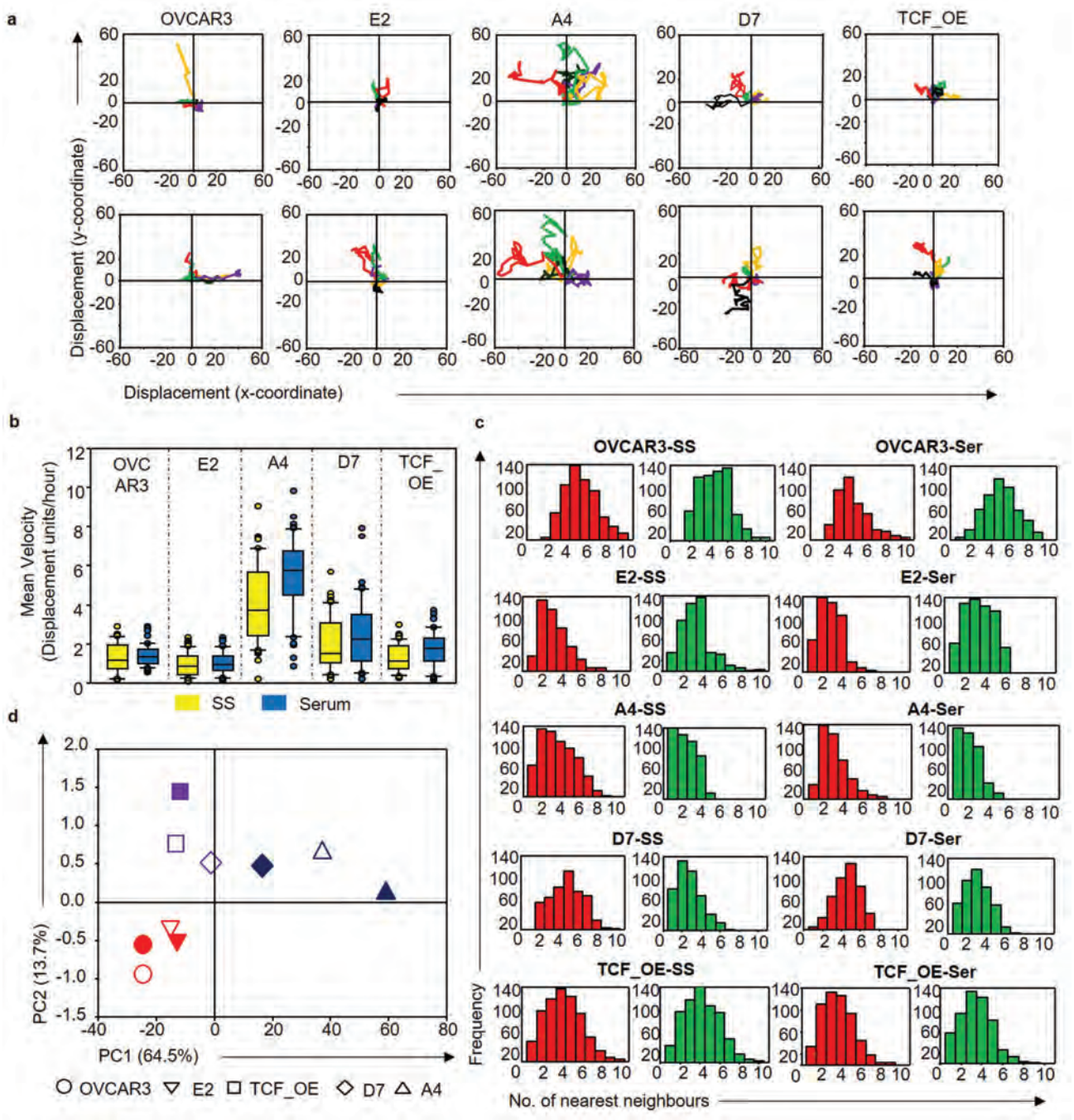

Figure 2. Quantitative metrics for resolution of migratory modalities. (**a**) Trajectories depicting migration directionality for parental cell lines (OVCAR3/Tcf21^{native}, A4/Slug^{native}) and respective derivatives (E2/Tcf21$^{K/O}$, D7/Slug$^{K/O}$ and TCF_OE/Slug$^{K/O}$Tcf21^{OE}). Plots represent trajectories of five randomly selected cells; (**b**) Representative plots depicting mean migratory velocity of parental (OVCAR3, A4) and derivative cells (E2, D7, TCF_OE). Displacement and velocity were derived from 'x' and 'y' positional coordinates detected over a 16 h duration; (**c**) Frequency of Nn for parental cell lines (OVCAR3, A4) and derivative clones (E2, D7, TCF_OE) at 0 h (red) and 16 h (green) time points distribution graphs depict Nn data for 750 cells. Experiments were performed in the absence/presence of serum. All cells identified in the microscopic field as particles were analyzed for displacement, velocity and Nn. However, only data points inclusive of the 'X', 'Y' coordinates and Nn over the entire duration of 16 h were used for data representation and interpretation; (**d**) Principle component (PC) analysis of time-lapse imaging-based migration data of parental (OVCAR3, A4) and derivative cells (E2, D7, TCF_OE), PC1—variance between displacement (final Y) and velocity versus Nn, PC2—variance between displacement and velocity; color gradient depicts migratory modes, blue-EMT, purple-aCCM, red-pCCM; filled and empty shapes indicate presence and absence of serum, respectively.

resolved five phenotypic states through definitive correlations between E (Cdh1,Ck19), M (Vim,FAP) markers and TFs (Tcf21, Slug and Prrx1 isoforms 1a and 1b; Supplementary Figure S3c–e, available at *Carcinogenesis* Online; Prrx1a, Prrx1b transcripts—P1a, P1b, respectively, protein represented as Prrx1) (27). Nonavailability of isoform-specific Prrx1 antibodies restricted further definitive studies for this TF. OVCAR3, OVCA432 (high E, nuclear Tcf21, low P1a–P1b–nuclear Prrx1, low nuclear Slug) and OVMZ6 cells with an inverse profile defined the E and M ends of the spectrum. CAOV3 and

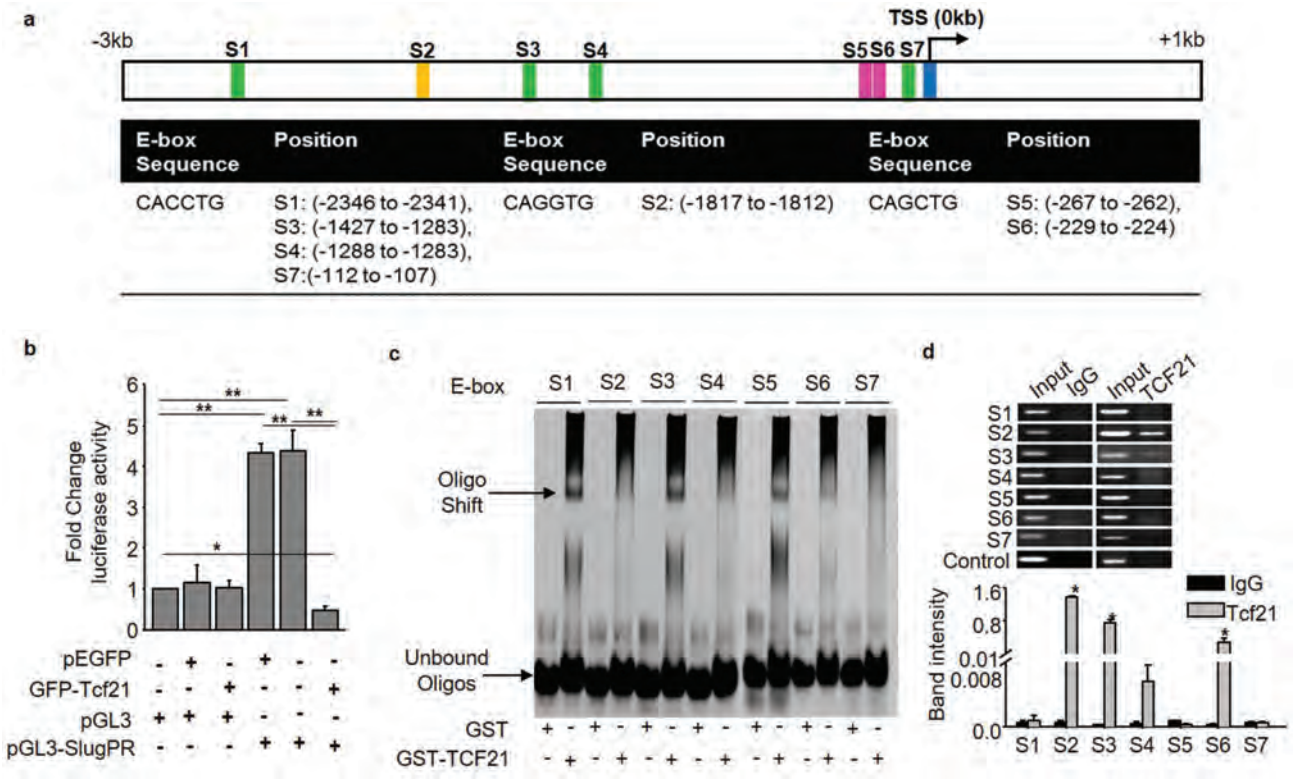

Figure 3. Tcf21-mediated Slug repression by direct promoter binding. (**a**) Schematic representation of Slug promoter region depicting the location and sequences of E-boxes. Promoter region: −3 kb to + 1 kb from transcription start site (TSS); (**b**) Reporter assays to determine effects of Tcf21 on wild type Slug promoter in A4 cells, luciferase activity normalized to untransfected cells; pEGFP: empty GFP vector, GFP–Tcf21: Tcf21–pEGFPC1 recombinant vector, pGL3: native luciferase vector, pGL3–SlugPR: pGL3 containing Slug promoter; (**c**) Representative EMSA of GST–Tcf21 recombinant protein binding to E-boxes in Slug promoter region in a cell free system, GST protein used as control; (**d**) ChIP–PCR analysis of Tcf21 binding to E-box elements in Slug promoter in OVCAR3 cells, IgG used as isotype control, cross-linked fragmented DNA considered as Input. All data are representative of experiments performed in triplicate and depicted as mean ± SEM. *P < 0.05, **P < 0.01, ***P < 0.001.

OV90 were identified as iE (high E, FAP, nuclear Tcf21, low P1a–P1b-moderate nuclear Prrx1, low nuclear Slug), OVCA420 and PEO14 as EM (E, M markers, all TFs in nucleus) and A4 as iM phenotype (CK19, M markers, low cytoplasmic Tcf21, high P1b, nuclear Prrx1 and Slug). These phenotypes could be perturbed by external stress such as serum deprivation that induced Cdh1 and nuclear Tcf21 expression, concomitantly decreasing Slug, FAP and Vim in the cell line panel to shift the spectrum toward the E phenotype (Figure 4a and b).

Probing phenotypic–functional associations assigned spheroid generation capabilities to intermediate states while E and M cells formed clumps/aggregates (Figure 4c). Except the E state, all cell lines were highly invasive in response to a serum gradient (Figure 4d). Differential migration capabilities were evident wherein A4, OV90 and OVCA420 cells filled the open wound area in absence of serum as opposed to E/iE and surprisingly M cells that required serum to achieve wound closure (Figures 4e.i and e.ii). Live imaging and PC analyses based on predefined quantitative metrics revealed pCCM in E and iE, aCCM in EM, coupling of aCCM–EMT in iM and EMT in M cells (Supplementary Video 2, available at *Carcinogenesis* Online; Figure 4e.iii). Interestingly, serum deprivation led to nuclear localization of Slug in a few EM state cells that possibly induces rare EMT events visualized in live imaging. Thus, the cell line panel reaffirmed existence of a phenotypic spectrum in HGSC defined by inherent Tcf21–Slug profiles and captured cellular plasticity as intermediate states following growth factor deprivation.

Microenvironment influenced phenotypic interconversions are captured by nuclear Tcf21 and Slug expression

Further examination of cellular plasticity across the EM axis and phenotype specific association of Tcf21–Slug, proceeded with exposure of the cell line panel and derivative clones to growth factors known to mediate directed phenotypic changes. TGFβ–BMP signaling plays a crucial role during ovarian/fallopian tube development and homeostasis. Additionally, the antagonistic influence of TGFβ1 and BMP7 on epithelial and mesenchymal phenotypes make them suitable triggers to assess HGSC cell line plasticity. E and iE cells were refractory in their response to both growth factors; BMP7 induced Cdh1, nuclear Tcf21 and reduced Slug levels whereas TGFβ1 exposure upregulated Slug concomitantly with reduced Cdh1 and Tcf21 in EM, iM and M cells (Figure 5a; Supplementary Figures S4a, S5a, and S6, available at *Carcinogenesis* Online). Dominant effects of BMP7 over TGFβ1 were observed in EM and iM cell lines (high Cdh1, nuclear Tcf21, low Slug) when the growth factors were provided in combination. Similarly, exposure of derivative clones (E2, D7 and TCF_OE) and parental cell lines (OVCAR3, A4) generated distinct responses that correlated with an inherent Tcf21–Slug balance. OVCAR3 cells were refractory to both growth factors while E2 responded poorly to BMP7 and exhibited enhanced nuclear Slug expression following exposure to TGFβ1. A4, D7, TCF_OE cells responded to BMP7 through nuclear localization of Tcf21, enhanced Cdh1 expression and reduced Slug. Conversely, TGFβ1 repressed Tcf21, Cdh1 in A4 and D7 cells with concomitant increase in Slug and Vim expression while TCF_OE

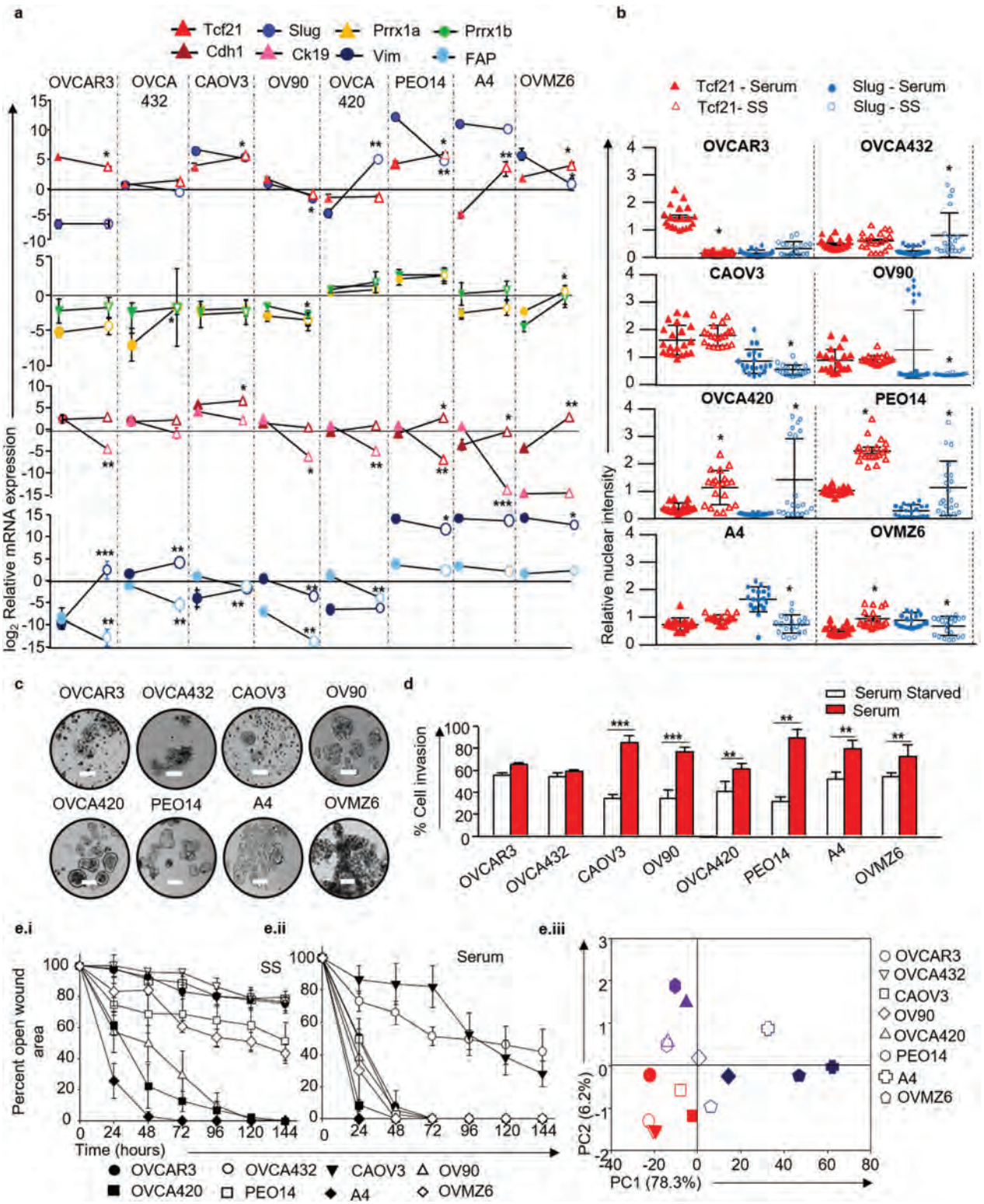

Figure 4. Resolution of the epithelial-mesenchymal phenotypic axis highlights differential functionalities as a function of Tcf21 and Slug localization. (**a**) Expression profiles of Tcf21, Slug, Prrx1 isoforms, Cdh1, Ck19, Vim and FAP in HGSC cell lines at steady states and post serum deprivation normalized with GAPDH. Filled shapes indicate the presence of serum and empty shapes indicate that cells were serum starved; (**b**) Representative graphs depicting frequency and intensity of Tcf21 and Slug positive nuclei in HGSC cell lines. Data depicts fluorescence intensities for each transcription factor measured across five random microscopic fields and quantified relative to the signal for Hoechst; (**c**) Representative images of suspension culture morphology (scale bars—200 μm); (**d**) Percent cell invasion in Boyden chamber matrigel assay in the absence and presence of serum; (**e**) Efficacy of wound healing in the (i) absence and (ii) presence of serum; (iii) Principle component analysis used to project segregation of migratory modes in the phenotypic spectrum based on quantitative metrics—final 'Y', velocity and Nn—emerging from time-lapse based migration data; color gradient represents the migratory modes of each cell line blue-EMT, purple-aCCM, red-pCCM; filled shapes indicate the presence of serum and empty shapes indicate that cells were serum starved. All data are representative of experiments performed in triplicate and are depicted as mean + SEM, $^{*}P < 0.05$, $^{**}P < 0.01$, $^{***}P < 0.001$.

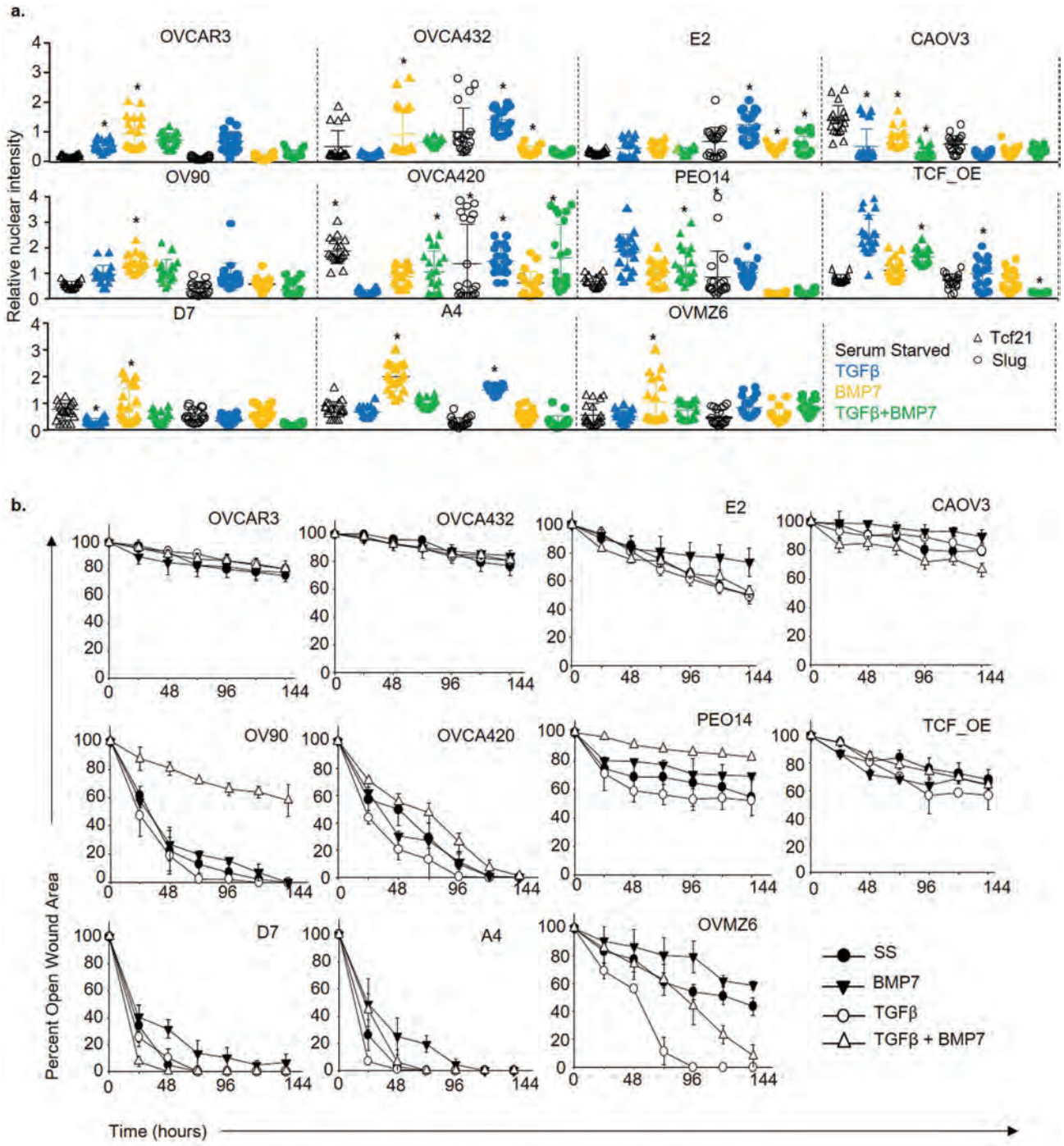

Figure 5. Tcf21/Slug subcellular localization correlates with HGSC wound healing efficacy. (**a**) Representative graphs depicting frequency and intensity of Tcf21 and Slug positive nuclei in HGSC cell lines and derivative clones (E2/Tcf21$^{K/O}$, D7/Slug$^{K/O}$ and TCF_OE/Slug$^{K/O}$Tcf21^{OE}) exposed to BMP7, TGFβ and BMP7 + TGFβ. Data depicts fluorescence intensities for each transcription factor measured across five random microscopic fields and quantified relative to the signal for Hoechst; (**b**) Graphical representation of wound healing efficiency of HGSC cell lines and derivative clones (E2, D7 and TCF_OE) following growth factor treatment as indicated; All data are representative of experiments performed in triplicate and depicted as mean ± SEM. *$P < 0.05$, **$P < 0.01$, ***$P < 0.001$.

responded poorly to the same (Figure 5a; Supplementary Figures S4b, S5b, and S6, available at *Carcinogenesis* Online). Thus, clone responses to combination of these two growth factors agreed with observations in the cell line panel. Integrating Tcf21 and Slug transcript profiles across all cell lines and derivatives under varying culture conditions (steady-state, serum-deprivation, growth factor exposure) with TF-promoter binding studies aided the generation of a mathematical model that identified TCF21^{high}–SLUG^{low} (E), TCF21^{low}–SLUG^{high} (M) and Tcf21^{mod}–Slug^{mod} (EM) as stable phenotypes while iE and iM were depicted as metastable states associated with phenotypic switches. Drastic fluctuations in Tcf21 and Slug expression correlated with transitions at the E and M ends, respectively (Supplementary Figure S4c, available at *Carcinogenesis* Online).

Functional evaluation of the microenvironmental influences revealed rate of wound closure to be restricted by BMP7 and enhanced by TGFβ in EM, iM and M, while minimal changes were evident in E and iE cells (Figure 5b). Combination treatment with both cytokines revealed a dominant effect of BMP7 over TGFβ in hindering wound closure. This functionality was altered in derivative clones wherein E2 exhibited moderately enhanced wound closure following exposure to TGFβ with minimal response to BMP7 in agreement with altered Tcf21–Slug balance; TGFβ enhanced and BMP7 reduced wound closure in D7 cells whereas TCF_OE exhibited minimal alterations. These observations assign cellular rigidity to E, M and plasticity to intermediate states. Conclusively, Tcf21–Slug expression and subcellular localization correlates with cellular states across the spectrum and are possible determinants of functionality in migration and phenotypic plasticity.

Drug-induced plasticity in HGSC associates with Tcf21–Slug crosstalk

Phenotypic plasticity in the EM spectrum was further assessed in response to a chemotherapeutic challenge (paclitaxel) and evaluated as a function of Tcf21–Slug expression. PC analysis of live migration derived metrics identified a switch from EMT to aCCM mode for M and iM cells after treatment (maximum variance along both PCs), EM and iE adhered to their characteristic modes of migration albeit at reduced velocities (moderate variance along both PCs) while pCCM phenotype in E cells was unaltered (Figure 6a; Supplementary Video S3, available at *Carcinogenesis* Online). These altered migratory metrics across the spectrum were associated with increased nuclear Tcf21 concurrently with reduced Slug expression (Figure 6b). Pacliaxel exposure induced an iE phenotype in E and iE cell lines, a similar shift toward the E phenotype was evident in EM, iM and M cells although the extent of each shift was distinct. To assign a mechanistic understanding to drug-induced phenotype switching, we probed occupancy of Tcf21 at the Slug promoter as a read-out of the E phenotype. Enhanced affinity of Tcf21 for the S2, S3 E-boxes in *SNAI2* promoter was identified following paclitaxel treatment and further complemented by negligent luciferase activity in Tcf21 overexpressing paclitaxel treated A4 cells (Figure 6c and d). Deletion of S2 E-box from the Slug promoter dramatically curbed Tcf21 mediated Slug

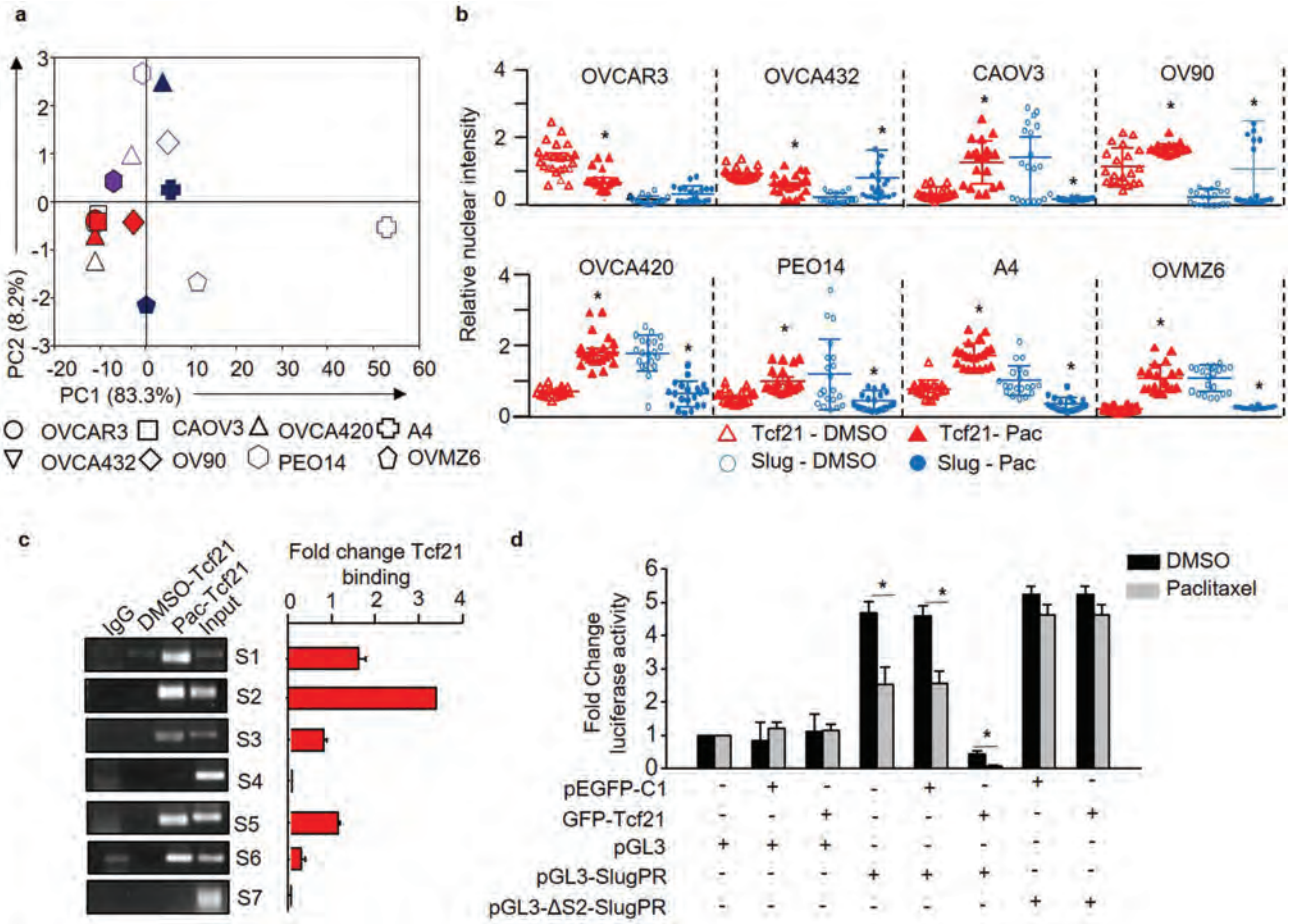

Figure 6. Class-switching in HGSC correlates with therapy induced Slug repression via Tcf21. a PC analysis used to project migratory modes of the different HGSC cell lines following paclitaxel exposure, PC1 and PC2 as described earlier; empty and filled shapes correspond to 0.1% DMSO and paclitaxel exposure, respectively in subsequent figures; (**b**) Representative graphs depicting frequency and intensity of Tcf21 and Slug positive nuclei in HGSC cell lines, data depicts fluorescence intensities for each transcription factor measured across five random microscopic fields following exposure to 0.1% DMSO (vector control)/paclitaxel (Pac) and quantified relative to the signal for Hoechst; (**c**) ChIP-PCR analysis depicting enrichment of Slug promoter regions in Tcf21 pulldown following paclitaxel exposure of A4 cells. IgG and DMSO used as isotype and vector control, respectively; (**d**) Reporter assays to determine effects of Tcf21 on wild type Slug promoter in A4 cells, luciferase activity normalized to untransfected cells. pEGFP: empty GFP vector, GFP–Tcf21: Tcf21–pEGFPC1 recombinant vector, pGL3: native luciferase vector, pGL3–SlugPR: pGL3 containing Slug promoter, pGL3–ΔS2–SlugPR: pGL3 containing Slug promoter with deleted S2 E-box. All data are representative of experiments performed in triplicate and are depicted as mean ± SEM. $^{*}P < 0.05$, $^{**}P < 0.01$, $^{***}P < 0.001$.

repression in the luciferase assay. These results together identify a Tcf21-driven phenotypic switch in HGSC cells that results in the emergence of epithelial traits.

Discussion

The anatomical proximity of ovarian surface and FT epithelium as sites of perturbed epithelial integrity, following ovulation and wound healing, have led to conflicting opinions on the cell-of-origin of ovarian cancer (14,28,29). The present study, restricted to the most aggressive subtype *viz.* HGSC, identifies Tcf21–Slug cross-talk in maintenance of intrinsic cellular states, wherein Tcf21-mediated Slug repression emerged as a feature of the epithelial phenotype. While previous studies exclusively implicate Slug as an EMT–TF (30), Tcf21 exhibits a tissue-specific activity in facilitating EM transitions. In the context of cardiac development, Tcf21 expression is linked with the onset of EMT in endocardial progenitors toward sculpting of the cardiac cushion and valves (31). Conversely, repression of this TF in renal and lung carcinomas results in overt metastasis, which can be suppressed through the activation of Kiss1, a tumor suppressor gene and target of Tcf21 (32,33). A balance of these TFs was associated with cellular plasticity as gauged by molecular and functional responses to extrinsic stimuli. Cells with native Tcf21 were conferred a highly rigid epithelial phenotype whereas dual nuclear positivity (Tcf21 and Slug) was associated with enhanced plasticity. Rigidity of epithelial and mesenchymal states was challenged by deriving intermediates (iE, EM, iM) and correlating phenotypes with discrete modes of migration despite comparable invasion (Supplementary Figure S7a, available at *Carcinogenesis* Online). The latter is thus underscored as a universal feature in HGSC and uncoupled from EMT (34).

Differential migration recapitulates events at the tumor edge (35,36), wherein destabilization of the tissue architecture by a degradative secretome and altered mileu may promote EMT, while exertion of tensile forces by adherens junction-linked acto-myosin complexes may induce CCM allowing invasion/deposition of tumor cells in the peritoneum (37–42). Our quantification of *in vitro* metrics, distinguished discrete migratory modalities across the phenotypic spectrum and correlated them with Tcf21–Slug expression. Application of live cell imaging also enhanced resolution of the *in vitro* wound healing assay, thus generating an improved informative method. Exploring the physiologically relevant BMP7–TGFβ signaling dynamics during ovulation (43–45), we identified the imposition of reduced migration with induction of nuclear Tcf21 and epithelial features through BMP7 exposure, while TGF-β enhanced EMT/aCCM mediated migration and mesenchymal features triggered by Slug expression (Supplementary Figure S7b, available at *Carcinogenesis* Online). While TGFβ has been extensively associated with HGSC pathology (46,47), previous reports on BMP7 have indirectly implied its role in therapy resistance, tumor progression and inhibition of TGFβ signaling in ovarian cancer (48–50). However, our findings conclusively identify a reciprocal role for these cytokines in governing cellular plasticity of ovarian cancer cells, which is reminiscent of their physiological activity during ovulation (45). These findings may be extrapolated to derive similarities between EMT–aCCM cooperation and OSE wound healing, while maintenance of the rigid, disparate epithelial state during pCCM could be akin to the FT-p53 signature-associated precursor lesions (51,52). Serum withdrawal as well as paclitaxel exposure promoted a Tcf21 driven epithelial state and induced aCCM that could represent a prosurvival mode of cooperative drug resistance. Moreover, Tcf21 expression associated with reduced sensitivity, and in return higher IC_{50}, of HGSC cell to the drug when tested across the HGSC panel (data not shown). Paclitaxel-induced shifts were further associated with Slug repression *via* direct promoter binding by the Tcf21. Interestingly, while the S2 E-box was most crucial for Slug inhibition, occupancy of multiple E-box sequences by Tcf21 may achieve a greater degree of inhibition. Previous studies on Slug auto-activation identified binding of the EMT–TF to the S2 E-box; thereby promoter occupancy by Tcf21 may prevent Slug–S2 interaction (18). Further support to these observations is provided by the de-repression of Slug promoter following S2 E-box deletion.

Although previous reports implicate Tcf21 as a tumor suppressor gene (53), our findings associate nuclear expression of this TF with therapy resistant populations and emphasize a tissue specific activity. Lack of linear correlations between mRNA and protein expression of these TFs along with dynamic alterations in subcellular localization highlight immense complexity of the Tcf21–Slug axis and warrant further studies pertaining to additional regulatory networks. Our findings also pose imminent questions regarding the epigenetic landscapes of the EM spectrum with respect to this axis; cellular compartment specific interacting partners of these TFs that assist their activity; mechanisms linking Tcf21–Slug to specific migratory modes; biochemical evaluation of protein domains responsible for differential subcellular localization, TF activity, and so on. A retrospective preclinical study from our group has further established Tcf21–Slug as potential biomarkers for HGSC tumor stratification and implied the adoption of tumor class-specific therapeutic regimes to effectively target the disease (54). Our report, thus supports this study and presents Tcf21–Slug as a crucial axis in HGSC cellular plasticity with genuine clinical implications.

Supplementary material

Supplementary data are available at *Carcinogenesis* online.

Funding

This work was supported by funding to S.A.B. from NCCS, Pune (intramural) and Department of Biotechnology, Government of India, New Delhi (extramural grants BT/IN/FINNISH/25/SB/2009, BT/Indo-Aus/06/03/2011). Research fellowships were availed as follows—S.S.V. from Council of Scientific and Industrial Research, New Delhi, India; M.M. from University Grants Commission, New Delhi India; B.K. from Department of Biotechnology, New Delhi, India; and A.A. from NCCS, Pune, India.

Acknowledgements

The authors acknowledge inputs from Ms Tejaswini Deshpande in bioinformatics analyses for generation of the TF network. We express our gratitude to Dr S. Mok (M. D. Anderson Cancer Center, TX) and Prof. Viktor Magdalen (Klinische Forschergruppe der Frauenklinik der TU München) for OV90 and OVMZ6 cell lines. We also extend our gratitude to Prof. Judith Clements (Translational Research Institute, Australia) for providing the OVCA420, PEO14, OVCA432 and CAOV3 cell lines. Matlab_r2013b for analysis of live cell imaging was provided by R.M. Deshmukh (National Centre for Biological Sciences, Bengaluru, India); Dr A. Karthick (NCCS, Pune, India) and V.K. Vittal (Indian Institute of Science Education and Research, Pune, India) provided expertise in live image processing.

Data availability

The authors declare that all relevant data supporting findings in this study are available within the article and its supplementary files. Data for quantitative metrics generated from live cell imaging data are available on request.

Conflict of Interest Statement: None declared.

References

1. Watson, C.J. *et al.* (2008) Mammary development in the embryo and adult: a journey of morphogenesis and commitment. *Development*, 135, 995–1003.
2. van Amerongen, R. *et al.* (2012) Developmental stage and time dictate the fate of Wnt/β-catenin-responsive stem cells in the mammary gland. *Cell Stem Cell*, 11, 387–400.
3. Gonzales, K.A.U. *et al.* (2017) Skin and its regenerative powers: an alliance between stem cells and their niche. *Dev. Cell*, 43, 387–401.
4. Proia, T.A. *et al.* (2011) Genetic predisposition directs breast cancer phenotype by dictating progenitor cell fate. *Cell Stem Cell*, 8, 149–163.
5. Guo, W. *et al.* (2012) Slug and Sox9 cooperatively determine the mammary stem cell state. *Cell*, 148, 1015–1028.
6. Varga, J. *et al.* (2017) Cell plasticity in epithelial homeostasis and tumorigenesis. *Nat. Cell Biol.*, 19, 1133–1141.
7. Nieto, M.A. *et al.* (2016) EMT: 2016. *Cell*, 166, 21–45.
8. Tan, T.Z. *et al.* (2013) Functional genomics identifies five distinct molecular subtypes with clinical relevance and pathways for growth control in epithelial ovarian cancer. *EMBO Mol. Med.*, 5, 983–998.
9. Huang, R.Y. *et al.* (2013) An EMT spectrum defines an anoikis-resistant and spheroidogenic intermediate mesenchymal state that is sensitive to e-cadherin restoration by a src-kinase inhibitor, saracatinib (AZD0530). *Cell Death Dis.*, 4, e915.
10. Tothill, R.W. *et al.*; Australian Ovarian Cancer Study Group. (2008) Novel molecular subtypes of serous and endometrioid ovarian cancer linked to clinical outcome. *Clin. Cancer Res.*, 14, 5198–5208.
11. Bell, D. *et al.* (2011) Integrated genomic analyses of ovarian carcinoma. *Nature*, 474, 609–615.
12. Yang, D. *et al.* (2013) Integrated analyses identify a master microRNA regulatory network for the mesenchymal subtype in serous ovarian cancer. *Cancer Cell*, 23, 186–199.
13. Kanchi, K.L. *et al.* (2014) Integrated analysis of germline and somatic variants in ovarian cancer. *Nat. Commun.*, 5, 3156.
14. Gardi, N.L. *et al.* (2014) Discrete molecular classes of ovarian cancer suggestive of unique mechanisms of transformation and metastases. *Clin. Cancer Res.*, 20, 87–99.
15. Domcke, S. *et al.* (2013) Evaluating cell lines as tumour models by comparison of genomic profiles. *Nat. Commun.*, 4, 2126.
16. Beaufort, C.M. *et al.* (2014) Ovarian cancer cell line panel (OCCP): clinical importance of *in vitro* morphological subtypes. *PLoS One*, 9, e103988.
17. Bapat, S.A. *et al.* (2005) Stem and progenitor-like cells contribute to the aggressive behavior of human epithelial ovarian cancer. *Cancer Res.*, 65, 3025–3029.
18. Kumar, B. *et al.* (2015) Auto-regulation of Slug mediates its activity during epithelial to mesenchymal transition. *Biochim. Biophys. Acta*, 1849, 1209–1218.
19. Kurrey, N.K. *et al.* (2009) Snail and slug mediate radioresistance and chemoresistance by antagonizing p53-mediated apoptosis and acquiring a stem-like phenotype in ovarian cancer cells. *Stem Cells*, 27, 2059–2068.
20. Naik, R.R. *et al.* (2016) A tumor deconstruction platform identifies definitive end points in the evaluation of drug responses. *Oncogene*, 35, 727–737.
21. Chen, Y. *et al.* (2018) Expression of transcription factor 21 (TCF21) and upregulation its level inhibits invasion and metastasis in esophageal squamous cell Carcinoma. *Med. Sci. Monit.*, 24, 4128–4136.
22. Mendez, M.G. *et al.* (2010) Vimentin induces changes in cell shape, motility, and adhesion during the epithelial to mesenchymal transition. *FASEB J.*, 24, 1838–1851.
23. Abid, M.R. *et al.* (2007) NADPH oxidase activity selectively modulates vascular endothelial growth factor signaling pathways. *J. Biol. Chem.*, 282, 35373–35385.
24. Roberts, E.W. *et al.* (2013) Depletion of stromal cells expressing fibroblast activation protein-α from skeletal muscle and bone marrow results in cachexia and anemia. *J. Exp. Med.*, 210, 1137–1151.
25. Hennessy, B.T. *et al.* (2009) Characterization of a naturally occurring breast cancer subset enriched in epithelial-to-mesenchymal transition and stem cell characteristics. *Cancer Res.*, 69, 4116–4124.
26. Rodler, D. *et al.* (2013) Expression of intermediate filaments in the Balbiani body and ovarian follicular wall of the Japanese quail (*Coturnix japonica*). *Cells. Tissues. Organs*, 197, 298–311.
27. Takano, S. *et al.* (2016) Prrx1 isoform switching regulates pancreatic cancer invasion and metastatic colonization. *Genes Dev.*, 30, 233–247.
28. Auersperg, N. (2013) Ovarian surface epithelium as a source of ovarian cancers: unwarranted speculation or evidence-based hypothesis? *Gynecol. Oncol.*, 130, 246–251.
29. Klotz, D.M. *et al.* (2017) Cells of origin of ovarian cancer: ovarian surface epithelium or fallopian tube? *Arch. Gynecol. Obstet.*, 296, 1055–1062.
30. Gasparics, Á. *et al.* (2018) MRTFs- master regulators of EMT. *Dev. Dyn.*, 247, 396–404.
31. Acharya, A. *et al.* (2012) The bHLH transcription factor Tcf21 is required for lineage-specific EMT of cardiac fibroblast progenitors. *Development*, 139, 2139–2149.
32. Arab, K. *et al.* (2011) Epigenetic deregulation of TCF21 inhibits metastasis suppressor KISS1 in metastatic melanoma. *Carcinogenesis*, 32, 1467–1473.
33. Gooskens, S.L. *et al.* (2018) TCF21 hypermethylation regulates renal tumor cell clonogenic proliferation and migration. *Mol. Oncol.*, 12, 166–179.
34. Schaeffer, D. *et al.* (2014) Cellular migration and invasion uncoupled: increased migration is not an inexorable consequence of epithelial-to-mesenchymal transition. *Mol. Cell. Biol.*, 34, 3486–3499.
35. Klymenko, Y. *et al.* (2017) Heterogeneous cadherin expression and multicellular aggregate dynamics in ovarian cancer dissemination. *Neoplasia*, 19, 549–563.
36. Symowicz, J. *et al.* (2007) Engagement of collagen-binding integrins promotes matrix metalloproteinase-9-dependent E-cadherin ectodomain shedding in ovarian carcinoma cells. *Cancer Res.*, 67, 2030–2039.
37. Mitchell, C.B. *et al.* (2016) Cooperative cell invasion: matrix metalloproteinase-mediated incorporation between cells. *Mol. Biol. Cell*, 27, 3284–3292.
38. Kamble, S.C. *et al.* (2013) Stem cell and cancer stem cell games on the ECM field. *J. Cancer Stem Cell Res.*, 1, 1.
39. Sunyer, R. *et al.* (2016) Collective cell durotaxis emerges from long-range intercellular force transmission. *Science*, 353, 1157–1161.
40. Iwanicki, M.P. *et al.* (2011) Ovarian cancer spheroids use myosin-generated force to clear the mesothelium. *Cancer Discov.*, 1, 144–157.
41. Dong, Y. *et al.* (2013) Paclitaxel resistance and multicellular spheroid formation are induced by kallikrein-related peptidase 4 in serous ovarian cancer cells in an ascites mimicking microenvironment. *PLoS ONE*, 8, e57056.
42. Aiello, N.M. *et al.* (2018) EMT subtype influences epithelial plasticity and mode of cell migration. *Dev. Cell*, 45, 681.e4–695.e4.
43. Ehnert, S. *et al.* (2012) Transforming growth factor β1 inhibits bone morphogenic protein (BMP)-2 and BMP-7 signaling via upregulation of Ski-related novel protein N (SnoN): possible mechanism for the failure of BMP therapy? *BMC Med.*, 10, 101.
44. Zeisberg, M. *et al.* (2003) BMP-7 counteracts TGF-beta1-induced epithelial-to-mesenchymal transition and reverses chronic renal injury. *Nat. Med.*, 9, 964–968.
45. Ng, A. *et al.* (2015) Ovary and fimbrial stem cells: biology, niche and cancer origins. *Nat. Rev. Mol. Cell Biol.*, 16, 625–638.
46. Kohan-Ivani, K. *et al.* (2016) Role of dihydrotestosterone (DHT) on TGF-β1 signaling pathway in epithelial ovarian cancer cells. *J. Cancer Res. Clin. Oncol.*, 142, 47–58.
47. Rafehi, S. *et al.* (2016) TGFβ signaling regulates epithelial-mesenchymal plasticity in ovarian cancer ascites-derived spheroids. *Endocr. Relat. Cancer*, 23, 147–159.
48. Sunde, J.S. *et al.* (2006) Expression profiling identifies altered expression of genes that contribute to the inhibition of transforming growth factor-beta signaling in ovarian cancer. *Cancer Res.*, 66, 8404–8412.
49. Cheng, L. *et al.* (2010) Analysis of chemotherapy response programs in ovarian cancers by the next-generation sequencing technologies. *Gynecol. Oncol.*, 117, 159–169.
50. Zhang, S.T. *et al.* (2016) Identification of key genes associated with the effect of estrogen on ovarian cancer using microarray analysis. *Arch. Gynecol. Obstet.*, 293, 421–427.
51. Berry, N.B. *et al.* (2008) Ovarian cancer plasticity and epigenomics in the acquisition of a stem-like phenotype. *J. Ovarian Res.*, 1, 8.
52. Xian, W. *et al.* (2010) The Li-Fraumeni syndrome (LFS): a model for the initiation of p53 signatures in the distal Fallopian tube. *J. Pathol.*, 220, 17–23.
53. Maezawa, Y. *et al.* (2014) Loss of the podocyte-expressed transcription factor Tcf21/Pod1 results in podocyte differentiation defects and FSGS. *J. Am. Soc. Nephrol.*, 25, 2459–2470.
54. Kamble, S. *et al.* (2019) Clinical stratification of high-grade ovarian serous carcinoma using a panel of six biomarkers. *J. Clin. Med.*, 8, 330.